Arabian Journal of Chemistry (2021) **14**, 103175

King Saud University

Arabian Journal of Chemistry

www.ksu.edu.sa
www.sciencedirect.com

REVIEW ARTICLE

Progress of *3d* metal-doped zinc oxide nanoparticles and the photocatalytic properties

Omar Muktaridha [a], Muhammad Adlim [a,b,*], Suhendrayatna Suhendrayatna [c], Ismail Ismail [d]

[a] *Graduate School of Mathematics and Applied Science, Universitas Syiah Kuala, Darussalam Banda Aceh, 23111, Indonesia*
[b] *Chemistry Department, FKIP, Universitas Syiah Kuala, Darussalam Banda Aceh, 23111, Indonesia*
[c] *Chemical Engineering Department, Faculty of Engineering, Universitas Syiah Kuala, Darussalam, Banda Aceh 23111, Indonesia*
[d] *Physics Department, Faculty of Math and Natural Science, Universitas Syiah Kuala, Darussalam Banda Aceh, 23111, Indonesia*

Received 4 January 2021; accepted 18 April 2021
Available online 27 April 2021

KEYWORDS

Bandgap;
Blueshift;
Dopant;
Nanoparticle;
Redshift

Abstract Modification of ZnO by doping with *3d* metal has been intensively reported, and many interesting applications have been proven. This review elaborated the doping effect of the *3d* metal atom (Sc, Ti, V, Cr, Mn, Fe, Co, Ni, and Cu) on the bandgap of ZnO and their application. The review involved more than 190 articles on the *3d* metal-doped ZnO, introducing some fundamental theories, including doping types, nanoparticle synthesis methods, nanoparticle morphologies, and lattice size changes. The preparation methods of *3d* metal-doped ZnO and the particle morphology effect are elaborated before discussing the correlation between dopant characteristics (type, content, radii) and the bandgap and crystallite size properties. The review ended with the application and photocatalytic degradation for dye in the visible and ultraviolet irradiation.

Contents

* Corresponding author at: Graduate School of Mathematics and Applied Science, Universitas Syiah Kuala, Darussalam Banda Aceh, 23111, Indonesia.
E-mail address: adlim@unsyiah.ac.id (M. Adlim).

Peer review under responsibility of King Saud University.

Production and hosting by Elsevier

https://doi.org/10.1016/j.arabjc.2021.103175
1878-5352

1. Introduction

Zinc oxide (ZnO) is one of the interesting metal oxides because it has several advantageous properties such as antibacterial (Lima et al., 2014), cytotoxin (Andrade et al., 2017), sunscreen material (Smijs and Pavel, 2011), photocatalytic (Salah et al., 2016), and sensor (Kim et al., 2017). ZnO is a non-toxic material, relatively thermodynamically stable (Ashrafi & Jagadish, 2007). It has low solubility in water (K_{sp} = 6.8 × 10^{-17}), suitable for photocatalytic materials of waste treatment in humid and watery conditions. However, pure ZnO has a wide bandgap energy (E_g = 3.37 eV) and a large exciton binding energy (60 meV) that make less photocatalytic efficiency (Ciciliati et al., 2015). The bandgap energy was the minimum energy required for moving the electron from the ground state to the excitation state. The exciton binding energy is related to the energy involved in chemical bonding rupture to initiate a chemical reaction. ZnO also has a high rate of recombination between the electron (e^-) and hole (h^+), hence the less chance of electron transferred to other molecules during photoinduced redox reaction (Bousslama et al., 2017; Ba-abbad et al., 2013; Yi et al., 2014; Ciciliati et al., 2015).

Ultraviolet (UV) irradiation, which has high photon energy, is required to activate the ZnO in photodegradation reactions (Zhang et al., 2017). Pure ZnO has low photocatalytic properties with sunlight as the source of photon energy since sunlight only reaches about 4% of UV light/UV-A (λ = 315–400 nm) (Mahdavi and Talesh, 2017), and dominated by 42–43% of visible light (λ = 400–700 nm), which has lower energy. To overcome this constraint, ZnO is modified by several approaches, including by controlling the morphology and the size, coupling with other semiconductors to produce Z-scheme, and by doping with several elements to induce the electron delocalization, to modify electron pathways in the presence of the new band of the doped atom.

Doping is related to the intentional introduction of impurities into a pure material for modulating the new properties. The dopant (doping atom) might have features as an electron donor or an electron-acceptor that generates electron delocalization in the doped material. The dopant produces another band between the highest occupied molecular orbital (HOMO) and lowest unoccupied molecular orbital (LUMO). In the photocatalyst concept, which is usually using inorganic compounds, the HOMO and LUMO are known as valence band (VB) and conduction band (CB), respectively (Qi et al., 2017). The orbital of the modified atom usually occupies between VB and CB, which acts as an electron bridge to assist the electron excitation and slows down the recombination rate. Several dopants used to modify the ZnO are non-metal (N, C, S, etc.), transition metal (Co, Mn, Fe, etc.), or noble metals (Au, Ag, Pd, etc.) (Yi et al., 2014). Each individual of the dopant might give a unique characteristic to the host of photocatalyst properties.

The comparative studies of theoretical and experimental findings related to *3d* metal (Sc, Ti, V, Cr, Mn, Fe, Co, Ni, and Cu)-doped ZnO are rarely found in the publication. The review on transition metal-doped ZnO was relatively general and had not focused on 3*d* metal-doped ZnO (Singh et al., 2019a,b). Each metal dopant effect on ZnO has not been discussed comprehensively (Shohany & Zak, 2020). Most of the existing literature focused on modifying the dopant concentration, the annealing temperature, and co-doping with more than one dopant. A theoretical analysis of a band-structure-corrected theory related to the simultaneously the chemical trends for electronic properties, carrier doping, and magnetism of the effect of *3d* dopant reported by Raebiger et al. (2009), but they did not explicitly discuss the ZnO photocatalytic activity. Bandgap calculation through simulation shows that the dopant concentration strongly affected the bandgap (Korir et al., 2021). They predicted blueshift and redshift affected by each dopant, but it has not been confirmed with experimental fact. Therefore, the discussion of the theoretical aspect and the experimental data for *3d* metal doped-ZnO properties is still interesting to explore

Redshift in this paper is terminology to describe the energy change characteristic to longer wavelength as the dopant effect. The energy changes to a shorter wavelength is blueshift (Das, 2015), compared to pure ZnO bandgap. The redshift is a higher possibility active in visible light where the Blueshift characteristics tend to be active in UV light.

Zinc (Zn) is an element of the *3d* metals, which have relatively similar ionic radii to the dopant discussed in these articles since they are in the same row at the periodic table. The ionic radius is such an essential condition because the dopant will substitute the Zn in the ZnO host atom in the lattices (Srinivasulu et al., 2017). The dopant ions have different characteristics, such as none *d* electron (Sc^{3+}), nearly fully occupied *d* orbital (Cu^{2+}), single, and multiple oxidation states (Co, Fe, V, Mn), which their effect on the composite properties are also interesting to compare.

This review elaborates *3d* metal properties as the doping effect. The trend of feature changes focused on the bandgap

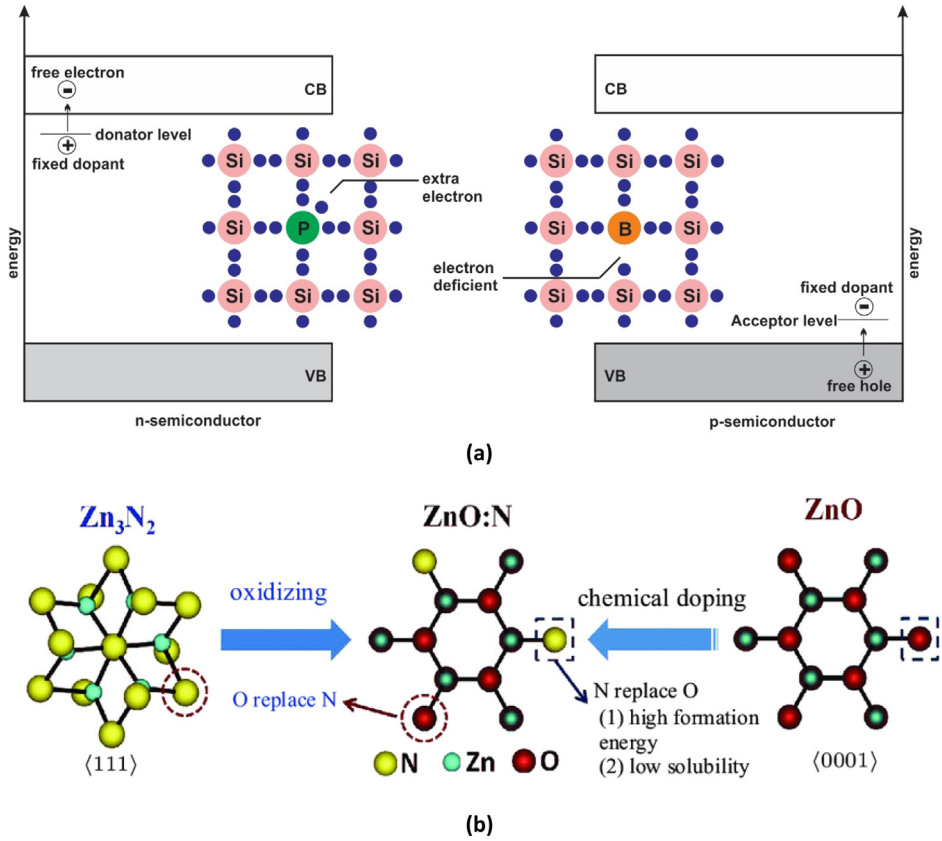

Fig. 1 (a). n- and p-type semiconductor of silicon (Si) doped, phosphorous (P) and boron (B), respectively (Cited from Tao, 2016) and reprinted from ((B. S. Li et al., 2017) Copyright belongs to Chinese Physical Society).

alteration, the particle morphology, and the applications. It elaborates on some basic terminologies and the purpose of doping, the type of doping that originates from semiconductor preparation. It introduces the trend of several doping methods that affect particle morphology. Most literature reported that the *3d* metal-doped ZnO is a photocatalyst for degrading dye pollutants in water. The application of a real-pollution-photo catalytic-removal, especially in the gas phase (such as volatile organic compounds, VOCs), is still scarcely discussed. State of the art is still interesting to explore.

2. Review methodology

We collected the related article from well-known publishers, including Elsevier, Springer Link, ACS publications, Tailor & Francis, MDPI, Hindawi, and The Royal Society of Chemistry. The qualitative (SEM, TEM) and quantitative (DRS, PL, XRD, UV–VIS) were collected from the primary article and compared each property base on the dopant (Sc, Ti, V, Cr, Mn, Fe, Co, Ni, and Cu) variable. Several review articles were also cited for expanding the data confirmation. The number of papers cited reached more than 190. The specific keyword used for Sc searching was "Sc doped ZnO for photocatalytic; the preparation and characterization of Sc doped ZnO". A similar way was applied for other metals. Other keywords were added, including "photodegradation, hydrothermal preparation for ZnO; sol–gel preparation for ZnO; co-precipitation preparation for ZnO". The potential article was collected based on 2010 to 2021.

We analyzed the preparation process (sol–gel, co-precipitation, and hydrothermal) at different dopants to study the effect on the particle morphology. The XRD crystallite size for each dopant was collected. It was correlated to the ionic radius to determine the shrinking and expanding crystallite size due to the doping process. The bandgap of each dopant was compared to search redshift and blueshift trends. The

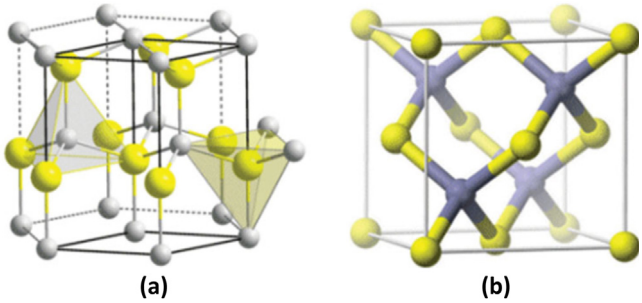

Fig. 2 The ZnO lattice structure of the atoms in (a) the wurtzite and (b) zinc blende, (reprinted from Aggarwal et al., 2018) Copyright belongs to Taylor & Francis.

photodegradation study on dye is collected from several different articles to explore UV and visible light use relevance.

3. Doping type of semiconductor

Doping is a popular topic in semiconductor technology, where silicon (Si) is doped with a dopant from two types of materials containing elements that are 3-valent (B, Al, or other) and 5-valent (P, As, Sb). The 3-valent dopant involves in p-type doping, and the 5-valent is categorized as n-type doping. As a typical dopant, phosphor has five valence electrons, and 4 of which will combine with 4 electrons of Si, and one is free to move and serves as a charge carrier, as displayed in Fig. 1 (a). It requires lower energy to move the electron from VB to CB. This type of dopant is known as an electron donor. Moving electron (negative charge) generates a positive charge into the lattice, and subsequently, another electron will move to a positive charge; thereby, cycle electron flow occurs. A reversed electron movement occurs in p-type doping. Boron has three valence electrons that will attract one electron from silicon, leaving a hole in the valence electron of silicon. The hole becomes a positive charge that makes another electron move into it and generates electron movement cycles (Fig. 1a).

ZnO is also a semiconductor material; its modification nearly similar to silicon. The bandgap alters as the effect of doping with several elements of metal and non-metal. Naturally, ZnO was an n-type semiconductor that can serve many electrons to share for other p-type semiconductors (Deng et al., 2021). However, doping with some elements can regulate the ZnO into the p-type semiconductor.

Typically, (Li et al., 2017a,b) described how to prepare n-type and p-type doping in ZnO. ZnO was doped with high electron density material such as group III (Al, Ga & In) or group VII elements to have n-type doping. For p-type doping, the Zn_3N_2 was prepared by thermal oxidizing (at 300–800 °C annealing temperature and oxygen atmosphere) to replace some N atoms with O atoms to form ZnO:N. Alternatively, conventional chemical doping, which is inserting N atoms from NH_3 gas into ZnO lattice in a nitrogen atmosphere, is illustrated (Chavillon et al., 2012) in Fig. 1 b.

Fig. 1**(b)**. Schematic diagram of p-type ZnO preparation either by oxidizing Zn3N2 (left arrow) or conventionally chemical doping (right arrow), (reprinted from Li et al., 2017a,b).

Ghahramanifard et al. (2018) and Sahal et al. (2016) reported the Cu-doped ZnO (p-type) was successfully synthesized through electrochemical deposition, where Cl-doped ZnO produces n-type ZnO. Also, the N-doped ZnO gave p-type ZnO (Ng et al., 2018 & Chavillon et al., 2012).

The most common ZnO structure is wurtzite (hexagonal lattice) and zinc blende (cubic lattice), as shown in Fig. 2. Wurtzite forms under normal conditions, but the zinc blende is synthesized at high pressure (Wu et al., 2008) and thin-film through spray pyrolysis (Muñoz-Aguirre et al., 2019). The lattice parameter of a and b was equal (2.249 Å) and c (5.206 Å) (Srinivasulu et al., 2017 & Sharma et al., 2020). As a semiconductor material, the ZnO VB is served by oxygen atoms from the 2*p* orbital, and the CB comes from the 3*d* orbital of the zinc atom (Qi et al., 2017). That condition is probably affected because the oxygen atom is more electronegative than the zinc, hence the low energy in the molecular orbital diagram.

Doping impurities of ZnO exhibits different characteristic bands depending on dopant type. The presence of metal in the ZnO lattice alters the electronic movement. Electron delocalization occurs due to the donor and acceptor electron properties of metal dopants and a new valence band from the non-metal dopants as presented in Fig. 3 (Chen et al., 2010 & Samadi et al., 2016). The presence of a new band in the bandgap energy level will reduce the bandgap significantly. Samadi et al., 2016 explained that the reduction potential based on Normal Hydrogen Electrode (NHE) of ZnO was more negative than that of the $O_2/\bullet O_2^-$. ZnO has the potential to release electrons to convert O_2 to superoxide anion radicals ($.\bullet O_2^-$). The hole (h^+) pulls an electron from H_2O and converts it into hydroxyl radical (•OH) since the NHE potential of $\bullet OH/H_2O$ is less positive than the valence band potential, as illustrated in Fig. 3.

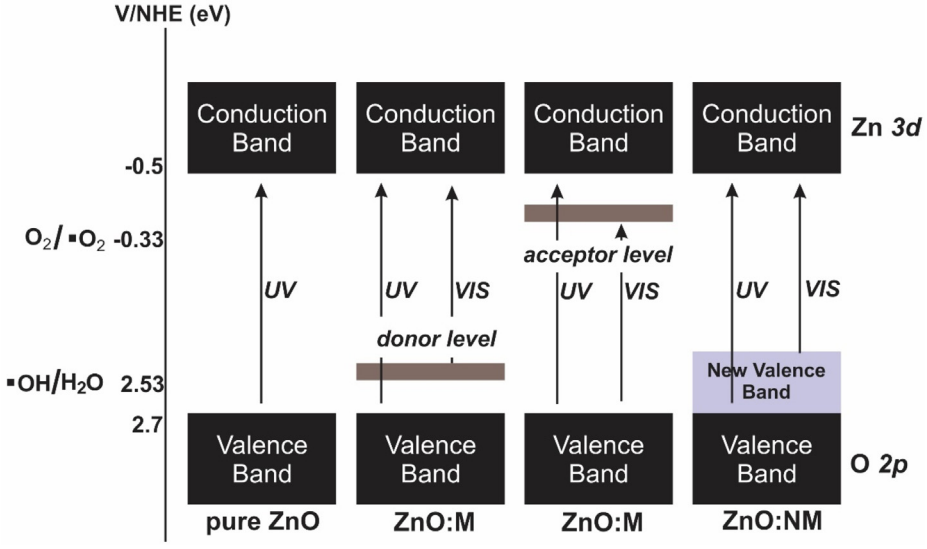

Fig. 3 The comparison of band theory of the pure ZnO, metal (M), and nonmetal (NM) doped ZnO (cited from Samadi et al., 2016; Qi et al., 2017; Chen et al., 2010; Raebiger et al., 2009 & Aliga et al., 2018).

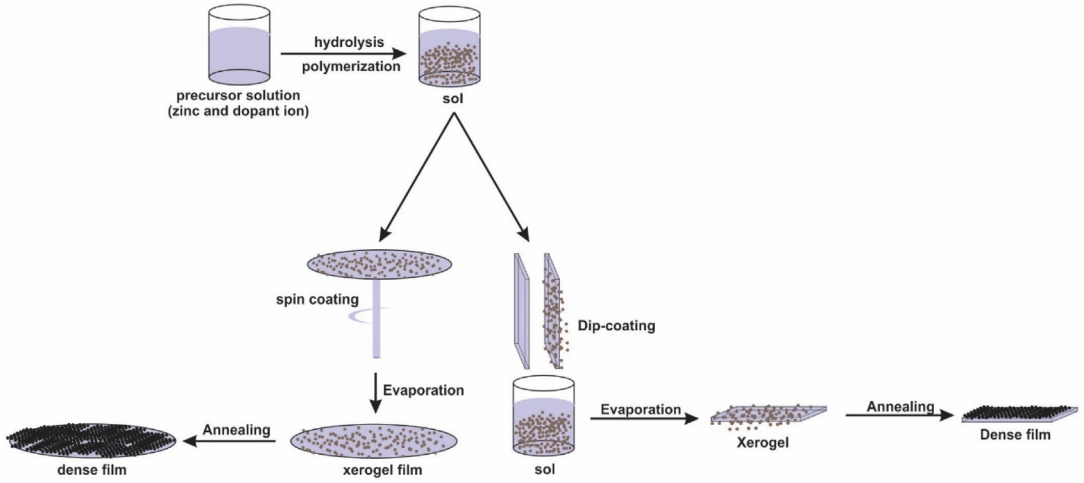

Fig. 4 The general route of the sol–gel preparation method for the dip and spin coating, (cited from Mahmood & Naeem, 2017 & Kumari et al., 2021).

4. Preparation methods of *3d* metal-doped ZnO and their morphological analysis

Before ZnO is recognized as a photocatalyst material, titanium dioxide (TiO_2) was previously popular in many photocatalysis research. It becomes a photocatalyst preparation material model. The doping process is carried out with several techniques, including sputtering, plasma, ion-implantation, chemical vapor deposition, hydrothermal, co-precipitation, and sol–gel (Wellia et al., 2011; Zhu et al., 2010 & Luo et al., 2012).

The preparation usually has two agendas: inserting dopants into the semiconductor lattices and attempting to obtain nano-sized particles with an average size of 1–100 (Zarlaida and Adlim, 2017). Therefore, nanoparticle preparation is also involved in the methods. The preparation methods are classified into two fundamental principles, which are the bottom-up and top-down mechanisms (Khan et al., 2019). The bottom-up technique synthesizes nanoparticles from the ions in a solution using a co-precipitation agent or physical heating with a chemical stabilizer to control their size since the crystal growth. The top-down technique involved changing a bulk material into a nano-size particle by grinding, milling, laser, and atomic evaporation.

We have reviewed the bottom-up technique and elaborated several applications of materials representing the nano-size properties (Zarlaida and Adlim, 2017 & Adlim, 2006). The sol–gel, solvothermal, hydrothermal, and co-precipitation methods are the most popular technique applied in ZnO nanoparticle preparations. Most of the methods used solvent, then it is known as a wet chemical method (Carofiglio et al., 2020). These methods involve relatively simple steps and adaptable for a specific purpose. Such as microwave heaters and ultrasonication stirrers regulate particle growth and morphology (Kumar et al., 2018).

4.1. Sol-gel methods

The sol–gel method is run at ambient temperature with a relatively simple process. Sol and gel are two different phase conditions, and the particles should be passed both of the states. Sol is a colloidal suspension containing microscopic particles and exhibits the Tyndall effect, and it looks like a solution. A gel is a colloid in the liquid medium, high viscosity, and it is somewhat a solid appearance. Usually, the sol is coated onto the support material and dried to form a xerogel by direct drying, especially in metal oxide preparation **(**Fig. 4**)**.

The sol solution contains a small suspension in a stabilizer solution, usually surfactant, amino acid, polymer, polysaccharide, and bio-extracts (Basnet & Chatterjee, 2020; Yusof et al., 2019). After the polymerization process, the sol matter coats

Table 1 Effect of sol–gel method of preparation on the morphology of ZnO nanoparticle.

Preparation description	D	Dispersion	Shapes	Reference
ethanol (s), ammonia (st), 600 °C-3 h (an)	Sc	Aggregated	Spherical	(Jiang et al., 2019)
methanol (s), 500 °C-2 h (an)	V	Aggregated	Spherical	(Slama et al., 2016)
N-dimethylformamide (s), 400 °C-12 h (an)	Mn	Aggregated	Hexagonal-spherical	(Mote et al., 2016)
water-isopropanol (s), 500 °C-4 h (an)	Mn	Aggregated	Spheroid-grain	(Kayani et al., 2020)
water (s), starch (st), 450 °C-5 h (an)	Fe	Aggregated	Granular-spherical	(Cherifi et al., 2016)
water (s), PVA (st), 400 °C (an)	Fe	Aggregated	Hexagonal-spherical	(Ciciliati et al., 2015)
2-Methoxyethanol (s), mono-ethanolamine (st), 650 °C-1 h (an)	Co	Aggregated	Hexagonal-spherical	(Caglar, 2013)
isopropyl alcohol (s), di-ethanolamine (st), 400 °C-2 h (an)	Co	Aggregated	Nearly spherical	(Poongodi et al., 2015)
ethanol (s), oxalic acid (st), 400 °C-2 h (an)	Co	Aggregated	Spherical	(Ba-Abbad et al., 2016)
ethanol (s), pH 9, 400 °C-3 h (an)	Ni	Aggregated	Nanorod-spherical	(Azfar et al., 2020)

s = solvent, st = stabilizer, an = annealing description, D = dopant

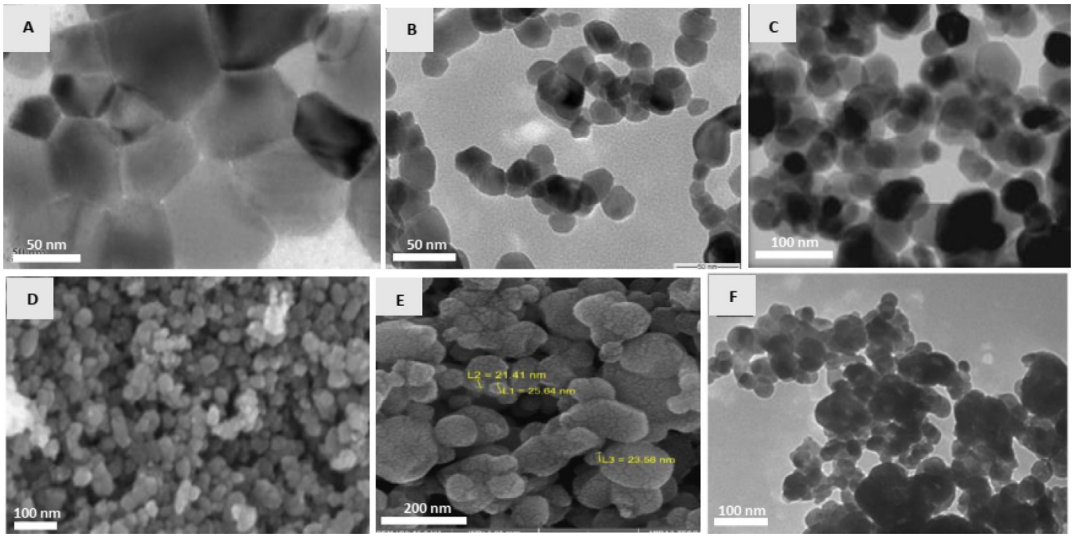

Fig. 5 Comparison of TEM and SEM images of 3d metal-doped ZnO morphology by sol–gel preparation, where the hexagonal-grain (A), spherical (B), grain-stick spherical (C), spherical (D), irregular grain (E), and hexagonal-spherical (F). (reprinted from Ciciliati et al., 2015; Slama et al., 2016; Khodadadi et al., 2016 & Alam et al., 2017) (Copyright belongs to Springer).

the surface of support materials and produces gel. The ZnO is prepared with a sol–gel process and subsequently heated with solvothermal or hydrothermal methods (Bai and Wu, 2011). According to several references as displayed in Table 1, such procedures seem preferably produce spherical shape particles immobilized onto the support material surface. Cited literature for *3d* metal-doped ZnO preparation with the sol–gel method is tabulated in Table 1**.**

ZnO aerogel was prepared by dehydrating the ZnO sol solution with the supercritical condition to produce much air space in their framework (Slama et al., 2016 & Bharat et al., 2019). Many other gel preparation processes have been discussed in the literature, including aerogel, xerogel, hydrogel, organogel, and ambigel. All types of gels are usually from the wet gel, and the drying steps are adjusted accordingly. As shown in Table 1, the sol–gel method tends to have aggregated particles. Most of the *3d* metal-doped ZnO nanoparticles synthesized by sol–gel methods are nearly spherical and rarely as nano-rod morphology (Yildirim et al., 2016). The TEM images of metal-doped ZnO particles prepared with sol–gel methods are displayed in Fig. 5.

4.2. Co-precipitation method

The co-precipitation method is also popular in ZnO nanoparticle preparation. Zn^{2+} from the precursor salt is precipitated out by the drop-added hydroxide ions (OH^-), and then the Zn $(OH)_2$ filtered, washed, purified, and dried. During precipitation, the solution is continuously stirring to avoid particle agglomeration (Margan and Haghighi, 2018). The co-precipitation process usually produces a unique morphology of the particles that depend on the synthesis condition. The particle morphology of ZnO nanoparticles prepared with co-precipitation methods is presented in Table 2**.**

Table 2 Effect of co-preparation method of preparation on the morphology of ZnO nanoparticle.

Preparation condition	D	Dispersion	Shape	Reference
Water (s), NaOH (b), PEG-6000 (st), 80 °C-overnight (dr)	Mn	Aggregated	Pyramid-spherical combination	(J. Singh et al., 2019a)
Water-2-mercaptoethanol (s), NaOH (b), 40 °C-30 min	Mn	Aggregated	Spherical-elongated	(Kalita and Kalita, 2019)
Water (s), NaOH (b), 700 °C-0.5 h (an)	Mn	Aggregated	Spherical-hexagonal	(Gao et al., 2016)
Water (s), NaOH (b), SDS (st), 300 °C-3 h (an)	Fe	Aggregated	Sea urchin-nanorod combination	(Hui et al., 2017)
Water (s), NaOH (b), PVP (st), 120 °C-2 h (dr)	Fe, Co, and Ni	Aggregated	Nano-rod	(Mondal et al., 2019)
water (s), KOH-pH 9.4 (b), 600 °C-2 h (an)	Ni and Co	Aggregated	Nano-rod	(Pascariu et al., 2018)
Water (s), NaOH-12 (b), twin-80 (st), 500 °C-2 h (an)	Ni	Slightly Aggregated	Sheet, rod, and spherical combination	(Fabbiyola et al., 2017)
Water (s), HMTA (b), PVP (st), 100 °C-8 h (dr)	Ni	Slightly Aggregated	Hexagonal-nanorod	(Thein et al., 2016)
water (s), NaOH (b), 450 °C, 8 h (an)	Cu	Aggregated	Nanorod-spherical combination	(Labhane et al., 2015)

s = solvent, st = stabilizer, an = annealing description, b = base, dr = drying, D = dopant

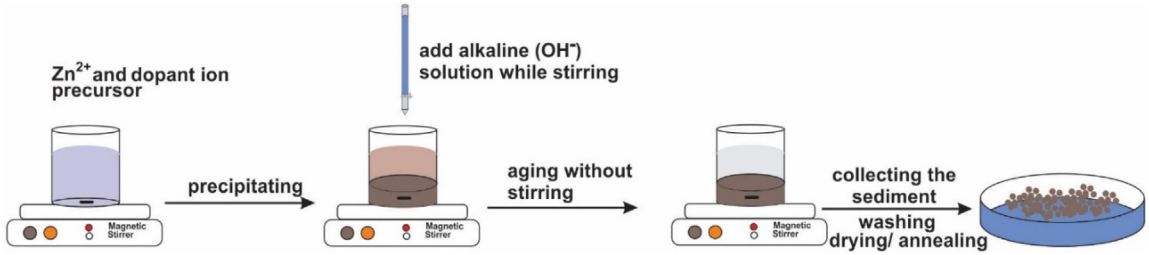

Fig. 6 The general route of the co-precipitation method (cited from Yuliarto et al., 2015).

The co-precipitation method is chosen to prepare powder metal-doped ZnO not. Still, the procedure is inappropriate for direct coating onto support material because the solution must be stirred during the precipitation process. In the co-precipitation method, the precursor solution is titrated with a precipitating agent, usually a base species, to form sediment of the zinc hydroxide ($Zn(OH)_2$). The precipitate of $Zn(OH)_2$ was washed and purified before calcinated in a furnace to produce zinc oxide (ZnO) (Fig. 6). In several conditions using alcohol as the solvent, base species (OH^-) are introduced into the Zn^{2+} ions, then ZnO directly formed by force hydrolysis (without annealing step). Such procedure prevents particle agglomeration as the heat effects (Rodriguez-Gattorno & Oskam, 2006; Klett et al., 2014).

From the literature listed in Table 2 and the image in Fig. 7, it can be inferred that co-precipitation methods tend to give rod shape ZnO nanoparticles, with a few are spherical and sea urchin shapes. Rod particles are probably produced during the formation of $Zn(OH)_2$ due to NaOH or other precipitate agents (Cao et al., 2019). Dopant atoms might affect the particle size, as reported by (Mondal et al., 2019). The concentration and rate of OH^- also affected the morphology because they are directed to anisotropic crystal growth. When both the precursors of OH^- and Zn^{2+} mixed simultaneously, the reaction became faster, but the particle morphology was controlled into nanosheet formation. When the addition of OH^- slows down, the morphology is becoming hexagonal prism (Ong et al., 2018).

Stabilizers probably also take a role in regulating particle morphology, as reported by (Basnet and Chatterjee, 2020). Sea urchin morphology was prepared using sodium dodecyl sulfate (SDS) as a stabilizer. SDS regulated the ZnO growth in one direction to give nanorod (Hui et al., 2017). In addition, the sea urchin morphology was a group of nanorods that are

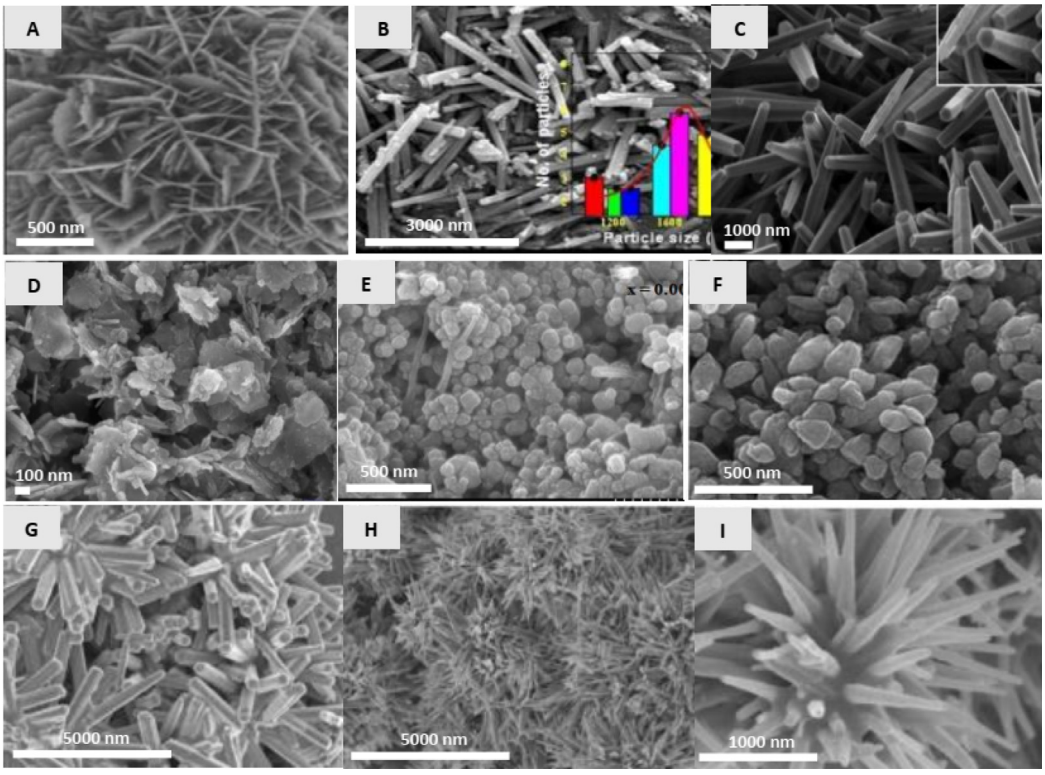

Fig. 7 *3d* metal-doped ZnO morphology synthesized by co-precipitation method, where the nanoflower (A), nanorod (B), nanorod (C), nanosheet-round (D), nanograin (E), nanopyramide (F) Nano sea-urchine (G, H, and I). (reprinted from Labhane et al., 2015; Hui et al., 2017; Thein et al., 2016; Rao & Vanaja, 2015; Ma et al., 2016 & J. Singh et al., 2019a) (Copyright belongs to Scientific Research Publishing).

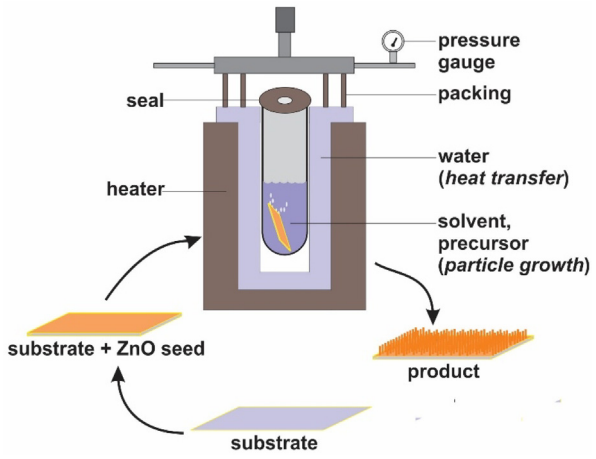

Fig. 8 Autoclave equipment for hydro/solvothermal reaction and the general route for the hydrothermal process (cited from Kominami et al., 2001 &Pimentel et al., 2016.

joined to the same nucleus so that it will form like a stick attached to a ball. PVP as a non-ionic polymer, the interaction during ZnO growth was directing the crystal growth toward the (0001) plane; hence the result was elongated morphology (Basnet and Chatterjee, 2020), and this also confirms by (Mondal et al., 2019), where the nanorod produced from the preparation process using PVP as capping agent.

4.3. Solvothermal method

Solvothermal is a general term for crystal formation reaction in solution using various solvents under supercritical or near supercritical conditions (Byrappa and Yoshimura, 1992). The specific term for the process depends on the solvent, where hydrothermal (water), glycothermal (glycol) (Beshkar et al., 2017), alcothermal (alcohol) (Muthukumar et al., 2020), ammonothermal (ammonia) (Grabianska et al., 2020), and so on.

In the laboratory, the solvothermal method usually used an autoclave to generate elevated temperature and pressure. Generally, the chemical reaction in the presence of a solvent (whether aqueous or non-aqueous) is run above the room temperature and at a pressure greater than 1 atm in a closed system (Yoshimura and Byrappa, 2008). The hydrothermal process is usually combined with another procedure like sol–gel and spray pyrolysis to spread the ZnO seed onto the support-materials surface. The metal-doped ZnO particles grow in high temperature and pressure (in an autoclave) within a stabilizer to regulate the size (Bai and Wu, 2011) (Fig. 8). The seeding process propagates a uniform nano-rod structure that can apply to sensor devices and photocatalysts.

Several studies on *3d* metal-doped ZnO nanoparticles synthesized by using hydrothermal are presented in Table 3. Solvothermal methods tend to grow the nanoparticles with a hexagonal-nanowire morphology, although some other shapes are also observed. Nanowire and nano-rods are relatively similar in shape, but nanowire has a longer length than nano-rods. The nano-rod and nanowire are usually produced when ZnO seed and Zn^{2+} ions are introduced into the autoclave. The seed will grow into a nano-rod or nanowire form (Fig. 9). The spherical particles existed when the synthesis was conducted without using ZnO seed, as reported by (Wojnarowicz et al., 2016). Nanoplate and nano-rod formed after Zn^{2+} ion precipitation and before heating into an autoclave, and such sequence will trigger ununiform morphology (Turkyilmaz et al., 2017; Yin et al., 2015).

5. Characteristic of *3d* metal-doped ZnO for crystallite size/structural analysis

The *3d* metals were scandium (Sc), titanium (Ti), vanadium (V), chromium (Cr), manganese (Mn), iron (Fe), cobalt (Co), nickel (Ni), copper (Cu), and zinc (Zn). Several of them have been reported as active dopants for ZnO. They are grouped as a transition metal, which partially filled the *d* sub-shell, except the Sc and Zn. The dopant precursors used in the synthesis process are usually the ionic high solubility salt. The dopant precursor usually has the same type of anion as the zinc precursor to minimize the impurity, and the anion shall be easily removed by heating or washing. Metal with nitrate (NO_3^-), sulfate (SO_4^{2-}), chloride (Cl^-), and acetate (CH_3COO^-)

Table 3 Effect of solvothermal method of preparation on the morphology of ZnO nanoparticle.

Preparation condition	D	dispersion	Shapes	Reference
Water (s), 120 °C, 20 h (ac)	Mn	Aggregated	Nanoplate-nanorod*	(Toufiq et al., 2021)
Water (s), 90 °C-6 h (ac)	Mn	Aggregated	Nanorod	(Raskar et al., 2019)
Water (s), 95 °C-6 h (ac)	Mn	Slightly aggregated	Nano-rod	(Putri et al., 2018)
Ethylene glycol (s), microwave 200 °C-25 min (ac)	Mn	Aggregated	Spherical*	(Wojnarowicz et al., 2016)
Water (s), 120 °C-20 h (ac)	Ni, Fe, and Mn*	Aggregated	Nanoplate-nanorod*	(Turkyilmaz et al., 2017) NaOH
Water (s), 95 °C-4 h (ac)	Fe	Slightly aggregated	Nanowire	(Habba et al., 2017)
Ethanol (s), 150 °C-24 h (ac), 60 °C-5 h (dr)	Co	Aggregated	Nanowire-nanorod	(Šutka et al., 2016)
Methanol (s), 200 °C-8 h (ac)	Ni	Aggregated	Hollow sphere*	(Yin et al., 2015)

s = solvent, st = stabilizer, ac = autoclave condition, dr = drying, D = dopant
* without using substrate/seed

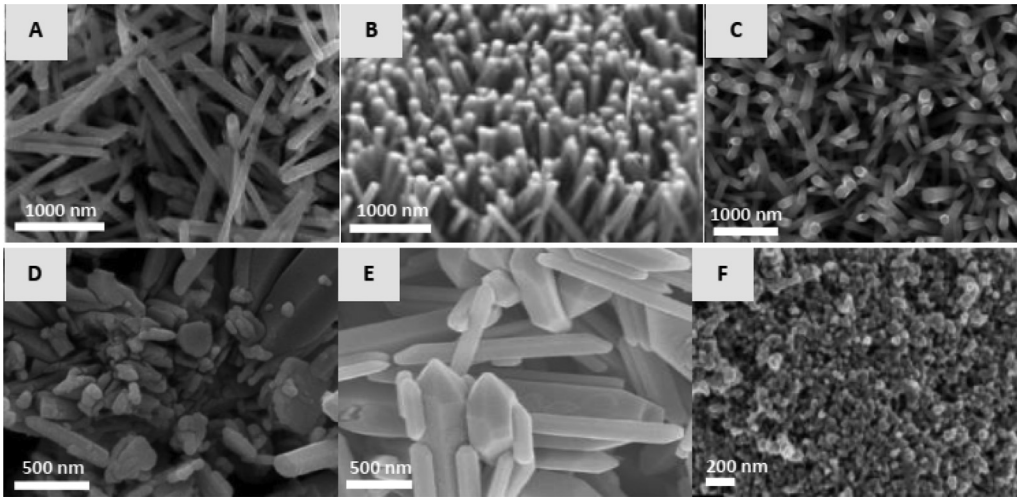

Fig. 9 **3d** metal-doped ZnO morphology synthesized by hydrothermal method, where the hexagonal nanowire (A), nanowire (B), nanorod (C), nanorod-nanoplate (D), hexagonal prismatic (E), spherical (F). (Reprinted from Šutka et al., 2016 ; W. Li et al., 2017 (Copyright belongs to MDPI); Turkyilmaz et al., 2017; Yin et al., 2015; Putri et al., 2018 & Wojnarowicz et al., 2016) (Copyright belongs to Beilstein).

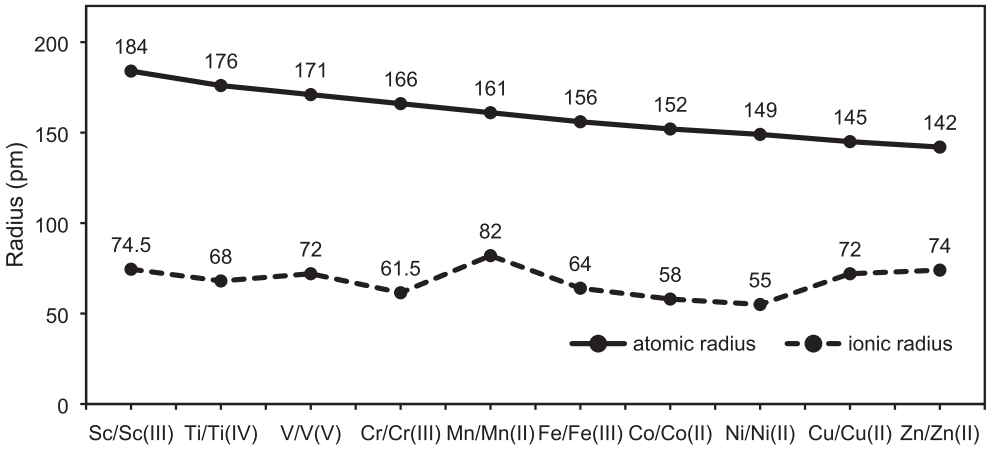

Fig. 10 Atomic and **the** ionic radius of the *3d* metal,(Cited from Miao et al., 2010; Bidier and Bououdina, 2017; Ghoul, 2016; Safa et al., 2018; Putri et al., 2018; Hui et al., 2017; Yildirim et al., 2016; Fabbiyola et al., 2017 & Kadam et al., 2017).

as anion usually are chosen as the precursor due to the ions are easily removed by heating. Titanium precursor is titanium tetra-isopropoxide (TTIP), titanyl acetylacetonate, or titanium (IV) butoxide.

The metals of *3d* block have moderate reactivity and possibly delocalize electrons**.** Atomic radii decrease along with the increasing atomic number, but the ionic radii are nearly similar in size to each other and much smaller than the atomic radii **(**Fig. 10**)**. The ionic radii are crucial for the doping process of ZnO. The dopant ionic radii must be smaller or at least equivalent to the radius of the Zn^{2+}. The oxidation state for each dopant doped to ZnO usually confirmed using X-ray Photoelectron Spectroscopy (XPS), as reported for Cr^{3+} (Nguyen et al., 2019), Mn^{2+} (Nithya et al., 2020), Fe^{3+} (Khan et al., 2020), Co^{2+} (Poornaprakash et al., 2020), Ni^{2+} (Xu et al., 2020), and Cu^{2+} (Jellal et al., 2021). Several other reports also stated that Sc^{3+} (Jiang et al., 2019), Ti^{4+} (Bidier et al., 2017), and V^{5+} (Fan et al., 2020).

Shrinking and expanding the lattice size is strongly affected by the presence of impurities in the lattice structure. The heterogeneous lattice strain broadens the peak and increases the Full Width at Half Maximum (FWHM) of the diffractogram. The FWHM enhancement affects the lattice size (Debye-Scherrer calculation). Lattice size expands significantly with the presence of the Mn^{2+} in the lattice, which causes the crystalline size enhancement, as tabulated in Table 4**.** Since Mn^{2+} ionic radii are bigger than that of Zn^{2+}, it probably expands the lattice size (Wang et al., 2020). The reversed trend is reported for smaller radii of 3*d* dopants, especially Ni^{2+}. A phenomenon on lattice size compression due to smaller dopant radii is known as compression stress by different ionic radii (Zhao et al., 2016). However, shrinking and expanding lattice size is not obvious if the size enlargement did not significantly different from ZnO nature lattice size. Fig. 11 shows the ZnO diffractogram before and after doped with the smallest and biggest ionic radii dopant.

Table 4 Effect of *3d* metal-doped ZnO on the crystallite size (0% doping belongs to ZnO crystal size).

Dopant	Synthesis method	Concentration (%wt)	The crystallite size (nm)	Reference
Sc	Sol-gel	0	21.50	(Yumak et al., 2015)
		1	20.34	
		2	16.47	
Ti	Hydrothermal	0	21.3	(Rahman et al., 2019)
		7.5	18.2	
V	Sol-gel combustion	0	56	(Gazzali et al., 2018)
		1	34	
		2	25	
		3	26	
		4	28	
Cr	Hydrothermal	0	57	(Debnath et al., 2019)
		3	44	
		5	35	
Mn	Sol-gel	0	21.8	(Khan et al., 2018)
		1	26.7	
		3	35.3	
Fe	Sol-gel	0	30	(Khan et al., 2020)
		2	30	
		4	27	
		6	23	
Co	Co-precipitation	0	42.90	(Pan et al., 2020)
		4	23.17	
		6	22.11	
		8	18.71	
Ni	Co-precipitation	0	45	Fabbiyola et al., 2017
		1	42	
		3	27	
Cu	Sol-gel	0	24.62	(Sajjad et al., 2018)
		1	21.62	
		2	19.61	

6. Characteristic of *3d* metal-doped ZnO for bandgap/ optical analysis

The bandgap is the crucial property for the semiconductor, and the bandgap is affected by the dopant. A theoretical study describes the effects of *3d* metal-doped ZnO on the properties of donor and acceptor electron representing the energy level. Such properties tend to be specific for each type of *3d* metal dopant, as illustrated in Fig. 12a. The effect of dopant (from Sc to Fe dopant) induces electron donor (blue line), but Co and Ni possibly caused electron acceptor (red line). The phenomenon is related to the charge transition properties. The splitting process also correlates to the charge transfer of metal-to-ligand charge transfer ($ML_{CB}CT$) and ligand-to-metal charge transfer ($L_{VB}MCT$), in which the host ZnO as a ligand and dopant as the metal (*d-d* transition) during pho-

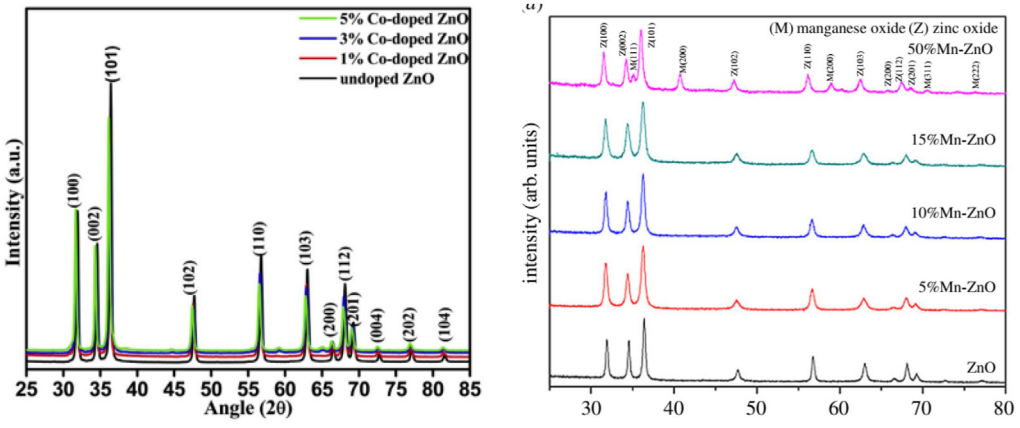

Fig. 11 **Diffractogram** of ZnO which doped by Co^{2+} (0.58 Å) and Mn^{2+} (0.82 Å) compare to Zn^{2+} (0.74 Å) (reprinted from Sahu et al., 2020 & Wang et al., 2020) (Copyright belongs to The Royal Society of Chemistry).

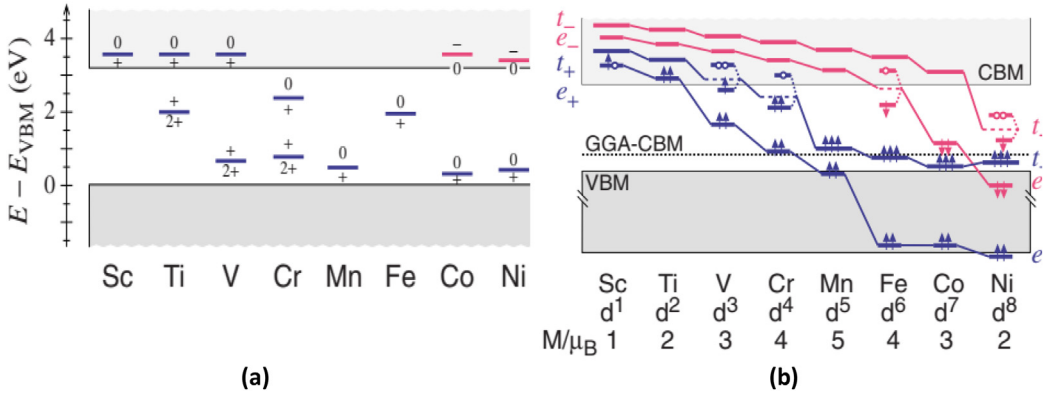

Fig. 12 (a) Donor and acceptor transition energies for *3d* metal-doped ZnO, where the blue and red lines denoted for donor and acceptor respectively (E = energy; E_{VBM} = energy of valence band minimum; eV = electron volt), (b) and *3d* metal-doped ZnO single-particle level configuration where the blue and red lines were high spin and low spin-orbital respectively (GGA = generalized gradient approximation; CBM = conduction band minimum; VBM = valence band minimum). (Reprinted from Raebiger et al., 2009) Copyright belongs to American Physical Society.

toexcitation occur(Samadi et al., 2016). The additional energy level of dopant is originated from the 3*d* orbital splitting since it introduces to the ZnO crystal, which has the tetrahedral geometry (orbital energy of $t_{2g} > e_g$) (Raebiger et al., 2009) & (Venkatesan et al., 2004), as shown in Fig. 12b. Fig. 12b shows that from Sc to Fe, the high spin-orbital (lower energy orbital) was dominated (blue line). Co and Ni dopant behave inversely (red line) or higher energy orbital, which is similar to the characteristic of π-acceptor ligand. It also relates to the increasing of the splitting gap gradually—this consistent with the Co and Ni acceptor level properties.

The comparison between *3d* metal-doped ZnO theoretical energy level and the experimental bandgap properties seems consistent (blue and redshift) as tabulated in Table 5. The trend correlates to the Fermi level and acceptor band of the theoretical studies. The presence of the donor band inside the conduction band shifts the Fermi level to the band, subsequently narrowing the bandgap through the Burstein-Moss effect. This theory likely occurs in Sc and Ti-doped ZnO (Table 5) (Yumak et al., 2015); (Chen et al., 2009); (Ye et al., 2013) & (Zhong and Zhang, 2013).

Sc-doped ZnO tends to widen the bandgap, as shown in Table 5, which might represent the Burstein-Moss effect. The Burstein-Moss effect occurs when the Fermi level lifts into the conduction band, which leads to the energy band broadening (Chen et al., 2009). This condition seems to confirm the theoretical analysis (Fig. 13a), where the donor level merges into the conduction band and subsequently affects the Fermi level. Dixon et al. (2017) recorded that Sc (less than 2%) caused widens the bandgap and gave a blueshift, but at higher Sc dopant (5%), it gave a redshift (Yumak et al., 2015). Since the bandgap narrowing correlates to the crystal defects, adding more dopant increases the defect and subsequently decreases the bandgap. Fig. 13 shows the effect of the Sc on the bandgap representing several reports. Since the dopant in low concentration, the bandgap was increased but decreased after 5%, probably related to the Urbach energy crystal disorder (Yumak et al., 2015 & Nurfani et al. 2021). Urbach energy is a parameter that is often associated with disordered, low, poor crystalline materials because of the localized states extended in the band gap (Anyaegbunam and Augustine, 2018).

Sc and Ti dopant (Table 5) show a blueshift effect consistent with the theoretical study that the donor level is merged into the CB, as the Burstein-Moss effects phenomena. The crystal defect, which is usually detected in the Raman spectra mode of E1(LO) around 576 cm, then disappeared after ZnO is doped with Ti (Tseng et al., 2012). Naeem et al. (2010) explained that the oxygen vacancies significantly increase with enhancing the Ti concentration. They also reported that bandgap widening occurs under low dopant concentration, but it decreases gradually due to dopant concentration enhancement. Ramadan et al. (2019) studied the Ti dopant effect on bandgap enhancement of Ti-doped ZnO at different annealing conditions, as presented in Fig. 14.

Research data show V-doped ZnO a redshift effect, as presented in Table 5. However, in the theoretical study, the V-doped ZnO still has a donor level that merges to the conduction band; the second donor level was close to the valence band, which can narrow the bandgap to assist electron excitation. The bandgap narrowing usually is affected by a crystal defect as a consequence of doping. Salah et al. (2016) recorded the Raman peak shifted at around 438.1 to 462,21 $cm^{-1,}$ which indicates the rigidity in the ZnO lattices in V^{5+} ion, as crystal defect tendency. The FT-IR spectra, where the stretching frequency of Zn-O bond at 485 cm^{-1} shifted significantly to 435 cm^{-1} due to 2% V dopant (Zhao et al., 2016). A few reports on the blueshift effect were also recorded, but the bandgap widening is not much significant difference. After 2% V-doped ZnO the bandgap changed from 3.23 to 3.24 eV (Tahir et al., 2009). A recent study also recorded the bandgap narrowed, as presented in Fig. 15.

Cr-doped ZnO characteristic is similar to that of V-doping, which is the redshift effect shown in Table 5. They are both reveal the position of donor level between the CB and VB (Raebiger et al., 2009). Density Functional Theory (DFT, a computerized quantitative calculation of the atomic electronic structure (Mazurek et al., 2020) shows substituting several Zn in ZnO lattices with Cr caused narrowing of the bandgap ZnO significantly from 3.39 into 2.71 eV (Meng et al., 2019).

The most common reason for restricting the bandgap was crystal defect enhancement due to introducing the impurities. The Gaussian fit of XPS analysis around 531 eV increased sig-

Table 5 Effect of *3d* metal-doped ZnO for the bandgap properties.

Metal Dopant	Bandgap	Application	Reference
Sc			
Sol-gel	Blueshift	Solar cell windows	(Sharma et al., 2009)
Sol-gel	Blueshift	Transparent semiconductor	(Chen et al., 2009)
Sol-gel	Blueshift	Transparent semiconductor	(Yumak et al., 2015)
Sol-gel	Redshift	Antibacterial	(Jiang et al., 2019)
Chemical vapor deposition	Blueshift	–	(Dixon et al., 2017)
Ti			
Hydrothermal	Blueshift	Optoelectronic	(Liu et al., 2013)
Hydrothermal	Blueshift	–	(Bidier and Bououdina, 2017)
Hydrothermal	Redshift	Electrode material	(Rahman et al., 2019)
Sol-gel	Blueshift	Biomedical devices	(Tseng et al., 2012)
Sol-gel	Blueshift	Electronic devices	(Ramadan et al., 2019)
Spray pyrolysis	Redshift	Photodegradation	(Rajasekaran et al., 2020)
V			
Hydrothermal	Redshift	Electronic devices	(Ramany et al., 2019)
Sol-gel	Redshift	Photodegradation	(Slama et al., 2016)
Sol-gel	Redshift	Photodegradation	(Ghoul, 2016)
Sol-gel	Redshift	–	(Bhardwaj et al., 2018)
Co-precipitation	Redshift	Photodegradation	(Djaja et al., 2020)
Microemulsion	Redshift	Optoelectronic devices	(Ali et al., 2019)
Solution combustion	Redshift	Spintronic, gas sensor	(Gazzali et al., 2018)
Cr			
Solvothermal	Redshift	Sensor, optoelectronic	(Iqbal et al., 2020)
Co-precipitation	Redshift	Photodegradation	(Djaja et al., 2016)
Co-precipitation	Redshift	Photodegradation	(Naz and Saeed, 2021)
Co-precipitation	Redshift	Antibacterial	(Rajivgandhi et al., 2021)
Sol-gel	Redshift	Photodegradation	(Hassan et al., 2015)
Sol-gel	Redshift	Photodegradation	(Nguyen et al., 2019)
Sol-gel	Redshift	Photodegradation	(Truong et al., 2019)
Auto combustion	Redshift	Spintronic	(Haq et al., 2018)
Mn			
Hydrothermal	Redshift	Photodegradation	(Putri et al., 2018)
Hydrothermal	Redshift	Photodegradation	(Raskar et al., 2019)
Hydrothermal	Blueshift	–	(Toufiq et al., 2021)
Sol-gel	Redshift	Photodegradation	(Kayani et al., 2020)
Sol-gel	Redshift	Photodegradation	(Khan et al., 2018)
Sol-gel	Redshift	Photodegradation	(Srinet et al., 2018)
Co-precipitation	Redshift	Photodegradation	(Das et al., 2020)
Co-precipitation	Blueshift	–	(Wu et al., 2019)
Co-precipitation	Blueshift	–	(Kalita and Kalita, 2019)
Co-precipitation	Blueshift	Photodegradation	(J. Singh et al., 2019a)
Co-precipitation	Blueshift	–	(Anju Chanu et al., 2019)
Electrospinning	Redshift	Photodegradation	(Wang et al., 2020)
Fe			
Hydrothermal	Redshift	Photodegradation	(Habba et al., 2017)
Co-precipitation	Redshift	Optoelectronic	(Saadi et al., 2020)
Co-precipitation	Redshift	Photodegradation, sensor	(Hui et al., 2017)
Sol-gel	Redshift	Photodegradation	(Khan et al., 2020)
Sol-gel	Redshift	Photodegradation	(Ong et al., 2019)
Sol-gel	Redshift	Photodegradation	(Han et al., 2019)
Sol-gel	Redshift	Photodegradation	(Bousslama et al., 2017)
Sol-gel	Redshift	Photodegradation	(Cherifi et al., 2016)
Pyrolysis	Redshift	Photodegradation	(Nurfani et al., 2021)
Co			
Solvothermal	Redshift	Photodegradation	(Šutka et al., 2016)
hydrothermal	Redshift	Photodegradation	(Poornaprakash et al., 2020)
Chemical bath deposition	Redshift	Optoelectronic	(Kaphle et al., 2019)
Sol-gel	Redshift	Photodegradation	(Yildirim et al., 2016)
Sol-gel	Redshift	Photodegradation, antibacterial	(Lima et al., 2014)
Sol-gel	Redshift	Photodegradation, antibacterial	(Poongodi et al., 2015)
Co-precipitation	Redshift	Photodegradation	(Pan et al., 2020)
Co-precipitation	Blueshift	–	(Sahu et al., 2020)

Table 5 (*continued*)

Metal Dopant	Bandgap	Application	Reference
Co-precipitation	Redshift	Photodegradation	(Devi and Velu, 2016)
Co-precipitation	Redshift	–	(Chithra et al., 2014)
Ni			
Sol-gel	Redshift	Photodegradation, solar cell	(Prerna et al., 2020)
Sol-gel	Blueshift	–	(Azfar et al., 2020)
Hydrothermal	Redshift	Photodegradation	(Xu et al., 2016)
Hydrothermal	Redshift	–	(Ma et al., 2020)
Hydrothermal	Redshift	Photodegradation	(Xu et al., 2020)
Chemical bath deposition	Redshift	Photodegradation	(Loyola Poul Raj et al., 2020)
Co-precipitation	Redshift	LED	(Kaur et al., 2019)
Co-precipitation	Redshift	Photodegradation, antibacterial	(Gnanamozhi et al., 2020)
Co-precipitation	Redshift	Photodegradation	(Thein et al., 2016)
Co-precipitation	Blueshift	Antibacterial	(Rana and Singh, 2016)
Co-precipitation	Redshift	Photodegradation	(Fabbiyola et al., 2017)
SILAR	Redshift	Sensor	(Amalraj et al., 2020)
Cu			
Hydrothermal	Redshift	Photodegradation	(Shah et al., 2020)
Hydrothermal	Redshift	Solar cell and photocatalyst	(Ben Saad et al., 2019)
Hydrothermal	Redshift	Photodegradation	(Hanh et al., 2019)
Hydrothermal	Redshift	Solar cell	(Ge et al., 2021)
Co-precipitation	Redshift	Photodegradation	(Sajjad et al., 2018)
Co-precipitation	Redshift	Optoelectronic	(Aneesiya and Louis, 2020)
Sol-gel	Redshift	Photodegradation	(Modwi et al., 2016)
Sol-gel	Redshift	Photodegradation	(Liau and Huang, 2017)
Spray pyrolysis	Redshift	Sensor	(Roguai and Djelloul, 2020)
Facile solution route	Redshift	Photodegradation	(Ma et al., 2019)
SILAR	Redshift	Photodegradation	(Jellal et al., 2021)

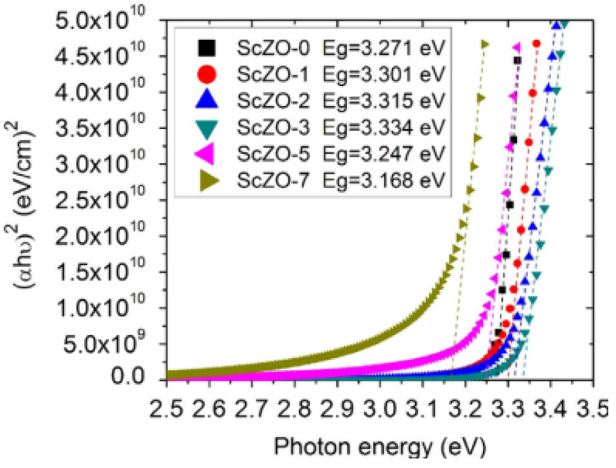

Fig. 13 Kubelka-Munk analysis for Sc-doped ZnO (reprinted from Yumak et al., 2015).

nificantly from 30.7 to 39.9 for 5%V-doped ZnO (Truong et al., 2019). Nguyen et al. (2019) also recorded the increasing Gaussian analysis of the XPS at around 531 corresponds to the oxygen vacancy after ZnO was doped by 1.38% Cr. The bandgap narrowed was also confirmed by a recent study as presented in Fig. 16.

Table 5 shows that Mn-doped ZnO exhibits mostly redshift properties, the crystal defect due to Mn present in the host lattices related to the bandgap properties. The photoluminescence (PL) data shows the defect of Zn interstitial (402 nm/ violet), oxygen vacancies (448–463 nm/ blue), deep interstitial oxygen states (482 and 525 nm/ green), and the oxygen interstitial (619 nm)/ orange) (Ma et al., 2016; Putri et al., 2018). Most of the crystal defects, especially oxygen vacancies, lead to decreased bandgap (Putri et al., 2018). (Samadi et al., 2016) also explained that the *d-d* transition in the crystal field by the presence of Mn-doped ZnO could induce visible-light irradiation. Although several publications also reported widening the bandgap due to the presence of MnO. The bandgap widens up to 4.2 eV responding to the excess Mn during the doping process (Gao et al., 2016; Ton-that et al., 2012).

In a nominally doped semiconductor, the Fermi level (the highest filled state) lies between the valence conduction band and valence band. As the doping concentration is increased, then electron populates states within the conduction band push the Fermi level to higher energy, which caused the bandgap to higher. This phenomenon is known as the Moss-Burstein effect or the Burstein-Moss shift (Gahlawat et al., 2019).

The Burstein Moss effect was a significant explanation since the MnO was not observed in the diffractogram. The phenomenon was explained through increasing electronic concentration in the conduction band after Mn substitution, hence pushing the Fermi level toward higher energy (Toufiq et al., 2021). The bandgap narrowing was also confirmed by a recent study, as like in Fig. 17.

Doping ZnO with Fe, which has a donor level, gives the redshift properties. Like most dopant effects, the Fe insertion into the ZnO lattice causes crystal defect, which affected the bandgap. Kanchana et al. (2016) reported from their photoluminescence (PL) spectra show the sharp peak at 412 nm related to zinc vacancies and at 522 nm related to oxygen vacancy.

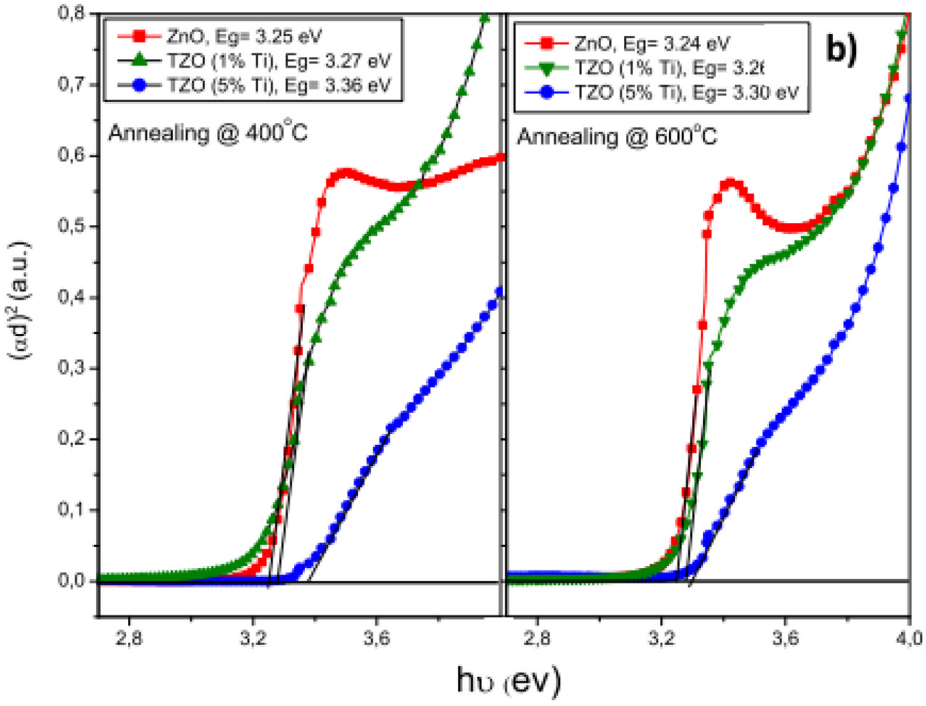

Fig. 14 Kubelka-Munk analysis for Ti-doped ZnO (reprinted from Ramadan et al., 2019) Copyright belongs to American Chemical Society.

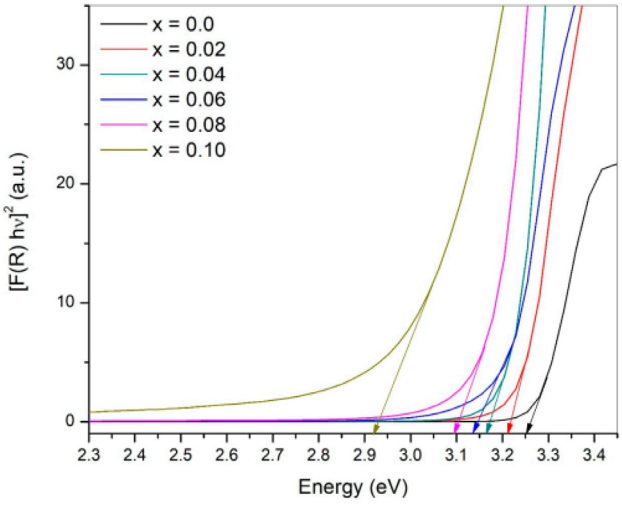

Fig. 15 **Kubelka**-Munk analysis for V-doped ZnO (reprinted from Ali et al., 2019) Copyright belongs to MDPI.

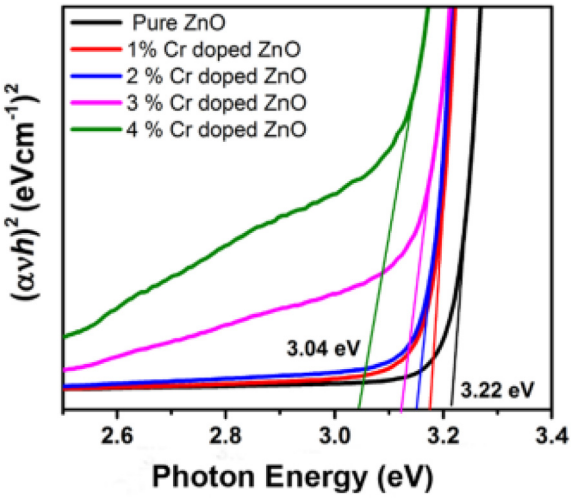

Fig. 16 **Kubelka**-Munk analysis for Cr-doped ZnO (reprinted from Iqbal et al., 2020).

Raman scattering shows the Fe-doped ZnO has many crystal defects, where the vibration mode around 656 cm^{-1} only appears due to Fe as the dopant (Yi et al., 2014). Mishra and Das (2010) recorded that the Fe-doped ZnO bandgap increased along with the dopant concentration. However, some literature shows the bandgap narrowing, as shown in Fig. 18. Additional defects occur, including the degenerate semiconductor due to too much dopant, and it leads to Burstein-Moss effects.

Theoretically, unlike other *3d* dopants, both Co and Ni have both donor and acceptor level properties, as discussed in Fig. 11. Table 5 experimental data show Co and Ni-doped ZnO mostly the redshift of the optical properties. There has not much explanation of the acceptor level effect on the experimental data. Lima et al. (2014) recorded the Urbach energy increased significantly follow the dopant concentration enhancement, which corresponds to the atomic structural disorder (Saadi et al., 2020). It was confirmed by the Raman spec-

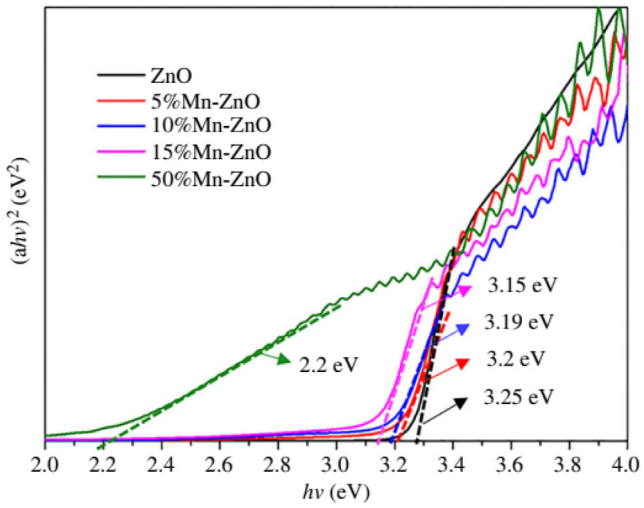

Fig. 17 Kubelka-Munk analysis for Mn-doped ZnO (reprinted from Wang et al., 2020).

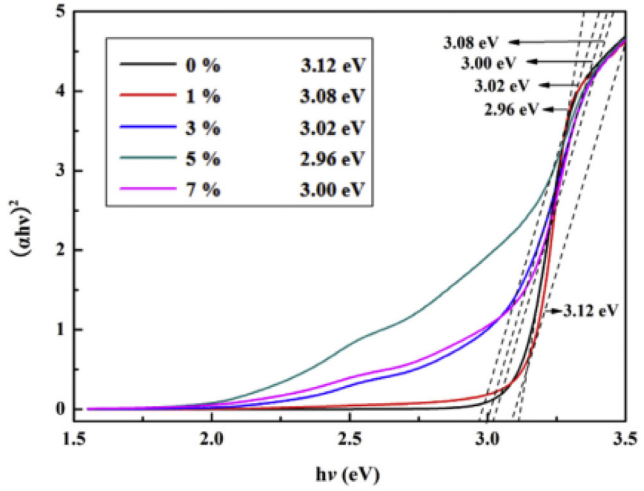

Fig. 18 Kubelka-Munk analysis for Fe-doped ZnO (reprinted from Hui et al., 2017).

tra that the vibration centered at 540 cm^{-1} correspondings to the donor defect bound on the Co site, which is related to the oxygen vacancy. Diffuse Reflectance Spectroscopy (DRS) analysis showed the photon absorption around the visible light, as represented by the addition peak of Co-doped ZnO around 569, 612, and 654 nm (Šutka et al., 2016). Most of the literature shows the Ni was present as Ni^{2+} instead of Ni^{0} (Xu et al., 2016). In this condition, it is possibly Ni^{2+} substituted some Zn^{2+} during the doping process, which enhances the formation of oxygen vacancies and additional energy levels and subsequently causes bandgap narrowing as predicted by Fabbiyola et al. (2017), and other factors might influence it. Although the NiO formed at excess Ni concentration, Ni-doped ZnO bandgap continuously decreased (Elilarassi & Chandrasekaran, 2011; Fabbiyola et al., 2017). One recent study also confirmed the bandgap narrowing due to the Co and Ni-doped, as in Fig. 19.

Table 5 shows Cu dopant properties follow the other *3d* metal that dominated with redshift properties. (Rooydell et al., 2017) already recorded that many crystal defects in the ZnO structure as exposed by the PL spectroscopy, but both of the doped and undoped ZnO exhibit two dominant peaks around the 372 nm as the near-band edge (NBE) and 425–650, which has green emission as the oxygen vacancies and zinc vacancies. They have also recorded the oxygen interstitial oxygen anti-sites, doped more than 8% of the Cu. The Raman spectrum also confirmed lattice distortion in the crystal that in the presence of Cu, it shifted the non-polar E2H mode from 431 to 422 cm-1 and decreased in the peak intensity (Iqbal et al., 2015). The Cu^{2+} and Zn^{2+} have similar ionic radii due to the neighboring atoms and enhance the substitution, which increases the oxygen vacancies to increase the crystal defects (Narayanan and Deepak, 2018). The bandgap narrowed of ZnO, which doped by Cu also confirmed in the recent study as in Fig. 20.

The comparison bandgap data of *3d* metal-doped ZnO at a given low concentration of various dopants are presented in Fig. 22. As shown, the bandgap tends to decrease from the Sc to Cu dopant. Increasing the dopant content tends to reduce bandgap, especially for Sc and Ti dopants due to the crystal disorder. The average bandgap of pure ZnO was about 3.27, which is smaller compared to the reported data bulk ZnO was 3.37 eV (Saadi et al., 2020). This condition is affected by

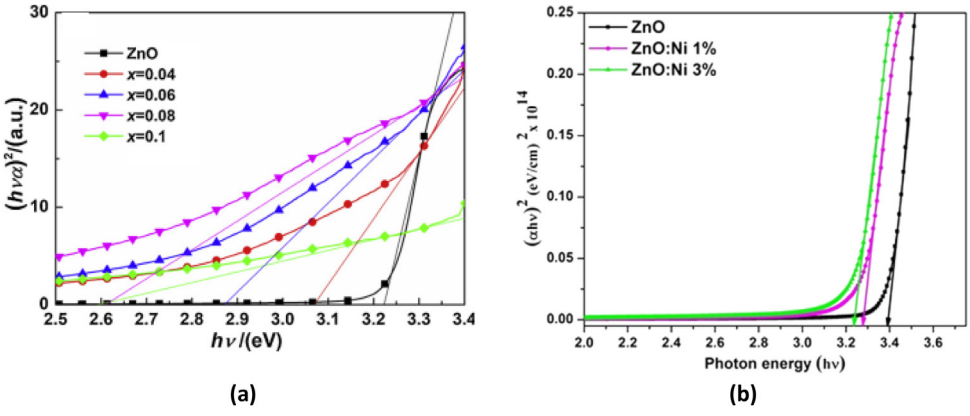

Fig. 19 Kubelka-Munk analysis for (a) Co-doped ZnO, and (b) Ni-doped ZnO (reprinted from Pan et al., 2020 & Loyola Poul Raj et al., 2020).

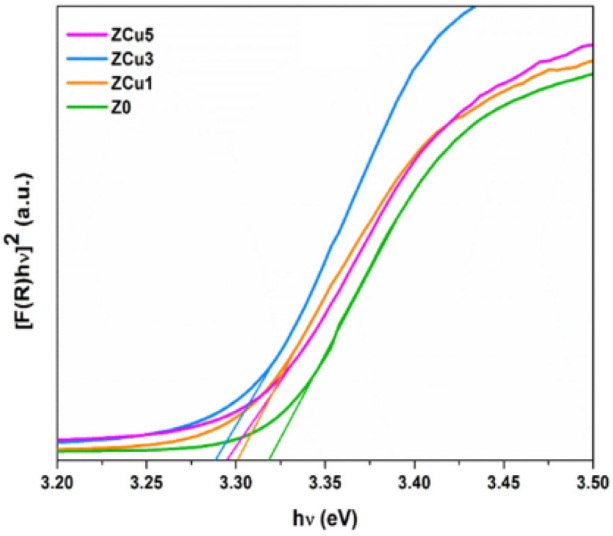

Fig. 20 Kubelka-Munk analysis for Cu-doped ZnO (Reprinted from Aneesiya & Louis, 2020).

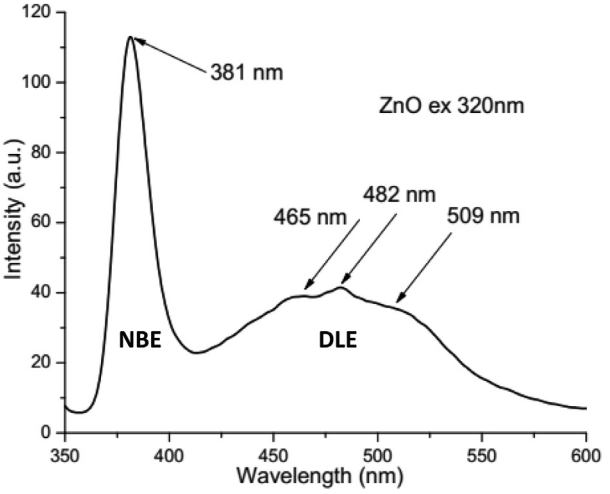

Fig. 21 Photoluminescence Spectrogram of pure ZnO with defect level of ultraviolet (381 nm) referred to Near Band Emission (NBE) and visible (465, 482, 509 nm) referred to the Deep Level Emission (DLE) (reprinted from Motelica et al., 2020b) Copyright belongs to MDPI.

the defect crystal during preparation, as observed by Motelica et al. (2020b), and they found a much smaller bandgap of 3.19 V. The crystal defect observed by using Photoluminescence instrument where the Near Band Emission (NBE) usually appear in the UV region with a sharp peak, and DLE in the visible region with broad peak (Sharma et al., 2020) as reported in Fig. 21.

A comparison of pure ZnO to the composite bandgap at a uniform concentration of dopant (±1%) is presented in Fig. 23. Sc has a significant blueshift effect, and Ti moderately behaves blueshift properties. The Sc and Ti dopant caused the composite to actively UV light. According to dopant type, starting from V to Cu, the impurities tend to give a redshift with various bandgaps. Except for Cr, Mn, and Ni, the other

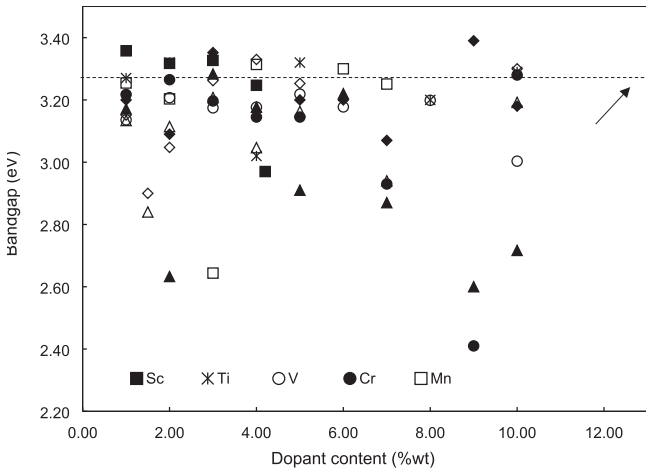

Fig. 22 The effect of dopant content on the bandgap of ZnO. Cited from: (Ciciliati et al., 2015; Bousslama et al., 2017; Cherifi et al., 2016; Poongodi et al., 2015; Ba-Abbad et al., 2016; Slama et al., 2016; Yildirim et al., 2016; Labhane et al., 2015; Ali et al., 2019; Bhardwaj et al., 2018; Bidier and Bououdina, 2017; Chen et al., 2009; Djaja et al., 2016; Fabbiyola et al., 2017; Ghoul, 2016; Habba et al., 2017; Hassan et al., 2015; Hui et al., 2017; Jiang et al., 2019; Kayani et al., 2018; Khan et al., 2018; Narayanan and Deepak, 2018; Putri et al., 2018; Ramadan et al., 2019; Ramany et al., 2019; Ray et al., 2016; Singh et al., 2019a; Slama et al., 2011; Tahir et al., 2009; Thein et al., 2016; Yumak et al., 2015; Ali et al., 2019; Ansari et al., 2012a,b; Arshad et al., 2011; Aydın et al., 2013; Basith et al., 2014; Devi and Velu, 2016; Dixon et al., 2017; Djaja et al., 2020; El-Ghoul et al., 2015; Haq et al., 2018; Iqbal et al., 2020; Jongnavakit et al., 2012; Kanchana et al., 2016; Raja et al., 2014; Rajasekaran et al., 2020; Sajjad et al., 2018; Srinet et al., 2018; Thennarasu and Sivasamy, 2016; Truong et al., 2019; Wu et al., 2019; Xu et al., 2016; Yu et al., 2014; Singh et al., 2019a; Wang et al., 2020; Raskar et al., 2019; Kayani et al., 2020; Saadi et al., 2020; Ong et al., 2019; Sahu et al., 2020; Pan et al., 2020; Xu et al., 2020; Ma et al., 2020; Amalraj et al., 2020; Aneesiya and Louis, 2020; Jellal et al., 2021; Hanh et al., 2019; Ge et al., 2021; Ben Saad et al., 2019; Roguai and Djelloul, 2020).

dopants have bandgap closely to be active in visible light. V, Co, and Cu dopants have the closest bandgap to be active in visible light, known as redshift effects. These data seem consistent with the experimental data (Qi et al., 2017) for Mn, Fe, Co, Ni, and Cu-doped ZnO. The data show the Mn, and Ni doping causes a slightly high bandgap, among others. The shifting bandgap relates to the energy required during photoexcitation. The redshift represents the lower energy requirement, and the blueshift the reverses condition.

Comparing to the computational data measured by (Korir et al., 2021) (Fig. 24), several dopants show a similar trend, especially for V, Mn, and Fe. But for Sc and Ti, most of the experimental studies show the bandgap widening (blueshift); however, there is a lack of research about the dopant, hence still need more confirmation. Also, several earliest study for Sc (Jiang et al., 2019) and Ti (Rahman et al., 2019; Rajasekaran et al., 2020) shows redshift effect. The Co, Ni, and Co dopant show inversely in the experimental study, even the earliest study report the redshift effect was observed by the Diffuse Reflectance Spectroscopy (DRS) and PL spectroscopy.

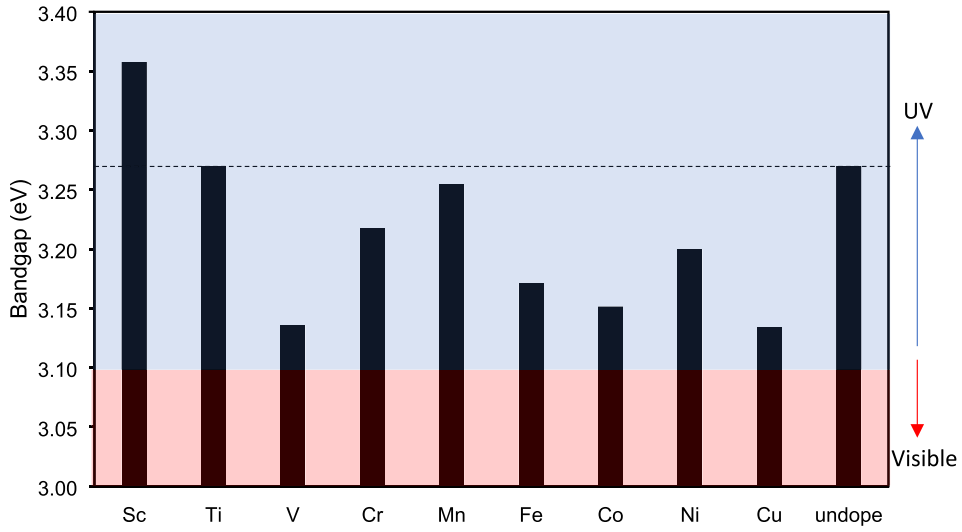

Fig. 23 The effect of dopant photocatalytic activity of *3d* metal-doped ZnO at 1%(wt) of dopant content, Cited from: (Abdel-wahab et al., 2016; Ba-Abbad et al., 2016; Bousslama et al., 2017; Cherifi et al., 2016; Ciciliati et al., 2015; Poongodi et al., 2015; Slama et al., 2016; Yildirim et al., 2016; Labhane et al., 2015; Ali et al., 2019; Ansari et al., 2012a,b; Bhardwaj et al., 2018; Bidier and Bououdina, 2017; Chen et al., 2009; Djaja et al., 2016; Fabbiyola et al., 2017; Ghoul, 2016; Habba et al., 2017; Hassan et al., 2015; Hui et al., 2017; Jiang et al., 2019; Kayani et al., 2018; Khan et al., 2018; Narayanan and Deepak, 2018; Putri et al., 2018; Ramadan et al., 2019; Ramany et al., 2019; Ray et al., 2016; Singh et al., 2019a; Slama et al., 2011; Tahir et al., 2009; Thein et al., 2016; Yumak et al., 2015; Ali et al., 2019; Ansari et al., 2012a,b; Arshad et al., 2011; Aydın et al., 2013; Basith et al., 2014; Devi and Velu, 2016; Dixon et al., 2017; Djaja et al., 2020; El-Ghoul et al., 2015; Haq et al., 2018; Iqbal et al., 2020; Jongnavakit et al., 2012; Kanchana et al., 2016; Raja et al., 2014; Rajasekaran et al., 2020; Sajjad et al., 2018; Srinet et al., 2018; Thennarasu and Sivasamy, 2016; Truong et al., 2019; Wu et al., 2019; Xu et al., 2016; Yu et al., 2014; Singh et al., 2019a; Wang et al., 2020; Raskar et al., 2019) (Kayani et al., 2020; Saadi et al., 2020; Ong et al., 2019; Sahu et al., 2020; Pan et al., 2020; Xu et al., 2020; Ma et al., 2020; Amalraj et al., 2020; Aneesiya and Louis, 2020; Jellal et al., 2021; Hanh et al., 2019; Ge et al., 2021; Ben Saad et al., 2019; Roguai and Djelloul, 2020).

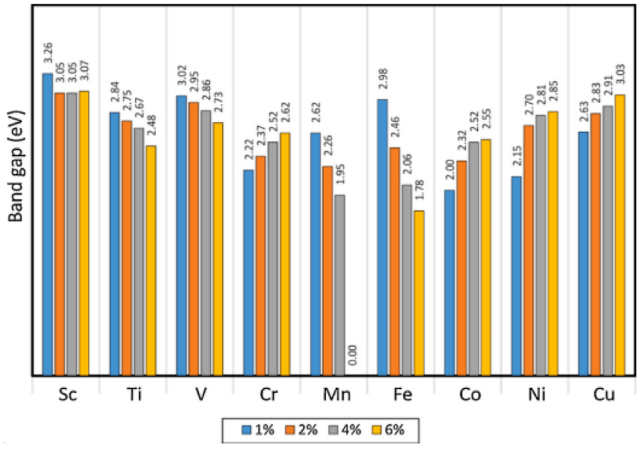

Fig. 24 Computational result the ZnO bandgap with varying the dopant concentration for 3*d* metal-doped ZnO (reprinted from Korir et al., 2021).

Fig. 25 compares the photoluminescence study on Ti-doped ZnO, which usually has blueshift effects and Cu-doped ZnO as the redshift representation. There are two significant peaks around ultraviolet wavelength (lower than 400 nm) as Near Band Emission (NBE) and visible wavelength (upper than 400 nm) as Deep Level Emission (DLE). The NBE peak of Ti-doped ZnO increased following the dopant concentration, which gives a blueshift effect. However, the DLE peak also rises due to the increasing the ZnO defect with introducing the dopant. Cu-doped ZnO shows the contras different properties, where the DLE band increased with more dopant and the NBE band decreased.

7. Application of zinc oxide modification for photodegradation

Photodegradation is one of the several applications of the ZnO as a semiconductor material. Photodegradation occurs involving radical molecules emitted from the redox photocatalytic reaction. The redox photocatalytic reaction extracted the electron (e^-) and hole (h^+) (Saharan et al., 2015). The e^- and h^+ react with the molecule in the environment (e.g., H_2O and O_2) to produce intermediate molecule (e.g., hydroxyl radical ($\bullet OH$) and oxygen radical ($\bullet O_2$) (Labhane et al., 2015). A possible reaction of the photocatalytic process is summarized in Table 6. The radical molecule is unstable because it loses an electron and attracts another electron from a nearby molecule.

Most photodegradation is carried out in the solution containing pollutants such as organic dye, microorganisms, etc. Photodegradation in the liquid phase usually involves water as the solvent since most of the research focuses on water treatment. Several parameters should be considered for maintaining the photodegradation for water treatment, such as the amount of catalyst, pH, light intensity, the concentration of pollutant, and so on. Also, the photodegradation rate depends on the degree of complexity of the pollutant molecule (Motelica et al., 2020a). The photodegradation activity of

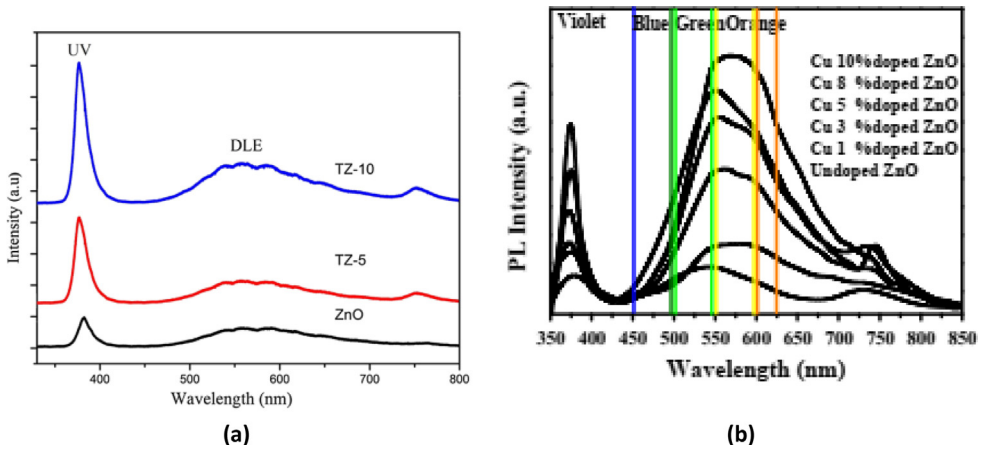

Fig. 25 Photoluminescence spectra of (a) Ti-doped ZnO (blueshift) and (b) Cu-doped ZnO (redshift) (reprinted from Bidier et al., 2017 & Rooydell et al., 2017).

Table 6 The propose of the possible photocatalytic reaction of ZnO and *3d* metal-doped ZnO involving radical molecule process.

(Undoped) ZnO + hν → h^+ + e^-			
Reaction with h^+		Reaction with e^-	
$h^+ + H_2O$	→ $H^+ + \bullet OH$	$O_2 + e^-$	→ $\bullet O_2^-$
$h^+ + OH^-$	→ $\bullet OH$	$\bullet O_2^- + 2H^+ + e^-$	→ H_2O_2
$H_2O_2 + 2\,h^+$	→ $O_2 + 2H^+$	$H_2O_2 + H^+ + e^-$	→ $\bullet OH + H_2O$
$H_2O_2 + \bullet OH/h^+$	→ $HO_2\bullet + H_2O/H^+$		
$HO_2\bullet + \bullet OH/h^+$	→ $O_2 + H_2O/H^+$		
Other reaction			
$\bullet OH + \bullet OH$	→ H_2O_2	$H_2O_2 + \bullet OH$	→ $HO_2\bullet + H_2O$
(doped) *3d* metal-doped ZnO + hν	→ **$h^+ + e^-$**		
Reaction with h^+	Reaction with e^-		
$h^+ + H_2O$	→ $H^+ + \bullet OH$	$O_2 + e^-$	→ $\bullet O_2^-$
$h^+ + OH^-$	→ $\bullet OH$	$\bullet O_2^- + 2H^+ + e^-$	→ H_2O_2
$H_2O_2 + 2\,h^+$	→ $O_2 + 2H^+$	$H_2O_2 + H^+ + e^-$	→ $\bullet OH + H_2O$
$H_2O_2 + \bullet OH/h^+$	→ $HO_2\bullet + H_2O/H^+$	$M^{p+} + e^-$	→ M^{r+}
$HO_2^{\cdot} + \bullet OH/h^+$	→ $O_2 + H_2O/H^+$		
$M^{p+} + h^+$	→ M^{q+}		
Other reaction			
$\bullet OH + \bullet OH$	→ H_2O_2	$H_2O_2 + \bullet OH$	→ $HO_2\bullet + H_2O$
$M^{p+} + O_2$	→ $M^{s+} + \bullet O_2^-$	$M^{p+} + OH^-$	→ $M^{t+} + \bullet OH$

methyl orange (MO) was eight-time higher than methylene blue (MB). The photodegradation also could break volatile organic compounds (VOCs) bond and decomposes them into smaller molecules such as CO_2 and H_2O (Kumar et al., 2014). The factor that affected photodegradation in the gas phase and within the solvent might be similar. Still, the humidity and abundant oxygen (airflow) will significantly influence (Shayegan et al., 2018). Also, the direct VOC degradation might not easily occur if the VOCs' reduction potential (V versus NHE) is outside range of ZnO reduction potential. The radical molecule/ reaction oxygen (ROS) species like •OH and $\bullet O_2^-$ behave antibacterial activity because of the ability to degrade the microorganism cell's organic molecule.

Photodegradation correlates with energy involvement and the catalyst bandgap. The Sc doped-ZnO was rarely used as photocatalyst material because it has a wide bandgap. Mn-doped ZnO was usually used ultraviolet light because it has a low redshift effect. Other *3d* metal-doped ZnO seem favorable to harvest the sunlight or other visible light sources (Table 7). Cu and Fe usually have good performance in visible light. Experts refer the Cu and Fe properties to their redshift effect (Table 5) and the UV and Visible catalytic degradation. Briefly, there is a tendency for 3*d* metal series dopants. The metals on the right side (the periodic table) are more receptive to visible light due to their relatively smaller bandgap than the left side metal. The blueshift dopant (Sc, Ti, and Mn) shall more compatible for fabric containing ZnO application to ovoid fabric decomposition. Their low activity in visible light and wide bandgap still absorbs UV light but less degrading properties.

Table 7 Summary of 3*d* metal-doped ZnO and their application for photodegradation.

Dopants, concentration (wt%)	Catalyst concentrations	Pollutants	Initial concentration (ppm); volume (mL)	Photon source	Efficiency (%); time (minutes)	Reference
Ti (7)	Powder, 3 g/L	MB	20 ; 100	UV	80; 120	(Darmadi et al., 2020)
V (3)	Powder, 0.5 g/L	MB	30; 150	Vis	100; 237	(Slama et al., 2016)
V(5)	Film, 4 × 25 cm	2-CP	20; NA	Sun	100; 240	(Salah et al., 2016)
Cr(4.5)	Powder, 1 g/L	MB	20; 50	UV	98; 150	(Chen et al., 2020)
Cr (3)	Powder, NA	MO	9.6; 200	Vis	40; 140	(Wu et al., 2011)
Mn (3)	Powder, 2g/L	O-II	10; 30	Sun	100; 270	(Achouri et al., 2016)
Mn (7)	Thin film, NA	MB	10; 20	UV	75; 40	(Putri et al., 2018)
Fe (5)	Powder, 0.1 g/ L	RhB	20; 50	UV	99; 100	(Hui et al., 2017)
Fe (1)	Powder, 0.1 g/L	MO	10; 60	UV	99; 120	(Yu et al., 2014)
Co (5)	Powder, 1 g/L	MO	10; 20	Vis	72; 300	(Šutka et al., 2016)
Co (3)	Thin film, NA	MB	12; NA	Vis	100; 120	(Yildirim et al., 2016)
Ni (7)	Thin film, NA	MG	3.64; 100	Vis	100; 240	(Abdel-wahab et al., 2016)
Cu (3)	Powder, 0.01 g/L	MO	9.8; 200	Vis	40; 140	(Wu et al., 2012)
Cu (1)	Powder, 3g/L	DB-71	10; 100	Vis	100; 120	(Thennarasu & Sivasamy, 2016)
Cu (0.5)	Thin film, NA	MB	3.2; 3	Vis	100; 360	(Jongnavakit et al., 2012)

UV = ultraviolet, Vis = visible lamp, Sun = sunlight, MB = methylene blue, DB = direct blue, MO = methyl orange, RhB = rhodamine B, AR = acid red, MG = methylene green, O = orange, CP = chlorophenol

8. Conclusions and outlook

Doping ZnO by *3d* metals has been reviewed to find out the trends of the properties and applications. Preparation methods of the metal-doped ZnO affect particle morphology. Sol-gel processes involving various dopants usually give spherical shape particles. Rod-like particles and nanowires are highly possible to obtain in co-precipitation procedures and hydrothermal methods, respectively. However, in the co-precipitation process, many particle morphologies were reported. The particle shapes were affected by many factors, including stabilizer, NaOH concentration, etc. The force hydrolysis method gave high dispersion particles without annealing.

The dopant ionic size is crucial for ZnO doping process because the suitable size dopant will substitute the host atom. The dopant atom radius usually induces the ZnO lattice size. Most of the 3d metal have smaller ionic radii comparing to the Zn, except for Mn. This condition seems to affect the crystallite size as reported that the expanding for Mn cases and shrinking for others but the doping processes are accomplished.

Sc and Ti doping on ZnO usually generate blueshift properties (short wavelength, wider bandgap). V, Fe, Ni, and Cu dopants have redshift characteristics (long wavelength, narrower bandgap). The *3d* metal-doped ZnO with redshift properties shall have better photocatalytic activity than the blueshift one. The redshift tends to be more active in visible light, where blueshift is preferably applied in UV light. Dopants with many oxidation states (Cr, Mn, Co) lead to activation in both blue and redshift.

Most of *3d* metals-doped ZnO are active in the photocatalytic due to the dopant effect. Decreasing the bandgap is followed by lowering photocatalytic reaction energy. In the photocatalytic process, *3d* metal-doped ZnO causes the emitting of unpair electrons that attack molecule water to generate free radical species. The free radicals degrade the pollutant molecules into smaller fragments and finally converted them into CO_2. Most of the photocatalytic studies reported are in liquid and few in the gas phase.

Declaration of Competing Interest

The authors declare that they have no known competing financial interests or personal relationships that could have appeared to influence the work reported in this paper.

Acknowledgment

Thanks to Universitas Syiah Kuala for PRUU-PD fellowship given to Muktaridha Omar, as a Ph.D student at the Graduate School of Math and Applied Science, Universitas Syiah Kuala Banda Aceh. PRUU-PD Research Grant # 292/UN11/SPK/PNBP/2020 Tanggal 24 Maret 2020 was awarded to Prof. M. Adlim, Ph.D, as the academic supervisor for Muktaridha Omar. Muktaridha Omar is the co-author of this paper.

References

Abdel-wahab, M.S., Jilani, A., Yahia, I.S., Al-ghamdi, A.A., 2016. Superlattices and Microstructures Enhanced the photocatalytic activity of Ni-doped ZnO thin films: Morphological, optical and XPS analysis. Superlattices Microstruct. 94, 108–118. https://doi.org/10.1016/j.spmi.2016.03.043.

Achouri, F., Corbel, S., Balan, L., Mozet, K., Girot, E., Medjahdi, G., Ben, M., Ghrabi, A., Schneider, R., 2016. Porous Mn-doped ZnO nanoparticles for enhanced solar and visible light photocatalysis. Mater. Des. 101, 309–316. https://doi.org/10.1016/j.matdes.2016.04.015.

Adlim, M., 2006. Review: Preparations and application of metal nanoparticles. Indo. J. Chem. 6, 1–10. https://doi.org/https://doi.org/10.22146/ijc.21785

Aggarwal, N., Vasishth, A., Singh, Bikramjit, Singh, Bhupinderpal, 2018. Investigation of room temperature ferromagnetic behaviour in dilute magnetic oxide. Integr. Ferroelectr. 186, 10–16. https://doi.org/10.1080/10584587.2017.1369317.

Alam, U., Khan, Azam, Raza, W., Khan, Abuzar, Bahnemann, D., 2017. Highly efficient Y and V co-doped ZnO photocatalyst with enhanced dye sensitized visible light photocatalytic activity. Catal. Today 284, 169–178. https://doi.org/10.1016/j.cattod.2016.11.037.

Ali, H., Alghamdi, A.S., Murtaza, G., Arif, H., Naeem, W., Farid, G., Sharif, S., Ashiq, M.G.B., Shabbir, S.A., 2019. Facile Microemulsion Synthesis of Vanadium-Doped. MDPI Mater. 12, 1–14. https://doi.org/10.3390/ma12050821.

Aliga, J., Cifuentes, N., Gonzalez, G., Sotomayor-Torres, C., Benevente, E., 2018. Enhancement Photocatalytic Activity of the Heterojunction of Two-Dimensional Hybrid Semiconductors ZnO/V2O5. Catalyst 8, 1–13. https://doi.org/10.3390/catal8090374.

Amalraj, A.S., Joycee, S.C., Rajah, A.J.L., 2020. Influence of Ni dopant on surface morphology of nanostructured ZnO thin films grown by SILAR method. Mater. Res. Innov. 24, 341–348. https://doi.org/10.1080/14328917.2019.1683697.

Andrade, L.J. De, Gonçalves, A., Vaulei, V., Mariucci, G., Carlos, A., Vianna, M., Vataru, C., Marcio, S., Humberto, L., Carla, J., Moraes, G., Adelina, A., Hechenleitner, W., Alfonso, E., Pineda, G., 2017. Effects of Al3+ concentration on the optical, structural, photocatalytic and cytotoxic properties of Al-doped ZnO. J. Alloys Compd. 729, 978–987. https://doi.org/10.1016/j.jallcom.2017.09.128.

Aneesiya, K.R., Louis, C., 2020. Localized surface plasmon resonance of Cu-doped ZnO nanostructures and the material's integration in dye sensitized solar cells (DSSCs) enabling high open-circuit potentials. J. Alloys Compd. 829. https://doi.org/10.1016/j.jallcom.2020.154497.

Anju Chanu, L., Joychandra Singh, W., Jugeshwar Singh, K., Nomita Devi, K., 2019. Effect of operational parameters on the photocatalytic degradation of Methylene blue dye solution using manganese doped ZnO nanoparticles. Results Phys. 12, 1230–1237. https://doi.org/10.1016/j.rinp.2018.12.089.

Ansari, S.A., Alam, F., Khan, A., Khan, W., Chaman, M., Muneer, M., Naqvi, H.A., 2012a. Influence of Cr Doping on the Microstructural, Optical and Photocatalytic Properties of ZnO Synthesized by Sol-Gel Method. Curr. Nanosci. 8, 581–586. https://doi.org/10.2174/157341312801784195.

Ansari, S.A., Nisar, A., Fatma, B., Khan, W., Naqvi, A.H., 2012b. Investigation on structural, optical and dielectric properties of Co doped ZnO nanoparticles synthesized by gel-combustion route. Mater. Sci. Eng. B 177, 428–435. https://doi.org/10.1016/j.mseb.2012.01.022.

Anyaegbunam, F.N.C., Augustine, C., 2018. A study of optical band gap and associated Urbach energy tail of chemically deposited metal oxides binary thin films. Dig. J. Nanomater. Biostructures 13, 847–856.

Arshad, M., Azam, A., Ahmed, A.S., Mollah, S., Naqvi, A.H., 2011. Effect of Co substitution on the structural and optical properties of ZnO nanoparticles synthesized by sol – gel route. J. Alloys Compd. 509, 8378–8381. https://doi.org/10.1016/j.jallcom.2011.05.047.

Ashrafi, A., Jagadish, C., 2007. Review of zincblende ZnO : Stability of metastable ZnO phases. J. Appl. Phys. 102, 1–12. https://doi.org/10.1063/1.2787957.

Aydın, C., El-sadek, M.S.A., Zheng, K., Yahia, I.S., Yakuphanoglu, F., 2013. Synthesis, diffused reflectance and electrical properties of nanocrystalline Fe-doped ZnO via sol-gel calcination technique. Opt. Laser Technol. 48, 447–452. https://doi.org/10.1016/j.optlastec.2012. 11.004.

Azfar, A.K., Kasim, M.F., Lokman, I.M., Rafaie, H.A., Mastuli, M. S., 2020. Comparative study on photocatalytic activity of transition metals (Ag and Ni)doped ZnO nanomaterials synthesized via sol–gel method. R. Soc. Open Sci. 7. https://doi.org/10.1098/rsos.191590.

Ba-abbad, M.M., Amir, A., Kadhum, H., Bakar, A., Takriff, M.S., 2013. Visible light photocatalytic activity of Fe3+ doped ZnO nanoparticle prepared via sol- gel technique. Chemosphere 91, 1604–1611. https://doi.org/10.1016/j.chemosphere.2012.12.055.

Ba-Abbad, M.M., Takriff, M.S., Benamor, A., Mohammad, A. W., 2016. Synthesis and characterisation of Co2+ incorporated ZnO nanoparticles prepared through a sol-gel method. Adv. Powder Technol. 27, 2439–2447. https://doi.org/10.1016/j.apt.2016.08.009.

Bai, S.-N., Wu, S., 2011. Synthesis of ZnO nanowires by the hydrothermal method, using sol-gel prepared ZnO seed films. J Mater Sci Mater Electron 22, 339–344. https://doi.org/10.1007/s10854-010-0139-2.

Basith, N.M., Vijaya, J.J., Kennedy, L.J., Bououdina, M., Jenefar, S., Kaviyarasan, V., 2014. Co-Doped ZnO Nanoparticles: Structural, Morphological, Optical, Magnetic and Antibacterial Studies. J. Mater. Sci. Technol. 30, 1108–1117. https://doi.org/10.1016/j.jmst.2014.07.013.

Basnet, P., Chatterjee, S., 2020. Structure-directing property and growth mechanism induced by capping agents in nanostructured ZnO during hydrothermal synthesis—A systematic review. Nano-Structures and Nano-Objects 22,. https://doi.org/10.1016/j.nanoso.2020.100426 100426.

Ben Saad, L., Soltane, L., Sediri, F., 2019. Pure and Cu-Doped ZnO Nanoparticles: Hydrothermal Synthesis, Structural, and Optical Properties. Russ. J. Phys. Chem. A 93, 2782–2788. https://doi.org/10.1134/S0036024419130259.

Beshkar, F., Khojasteh, H., Salavati-Niasari, M., 2017. Flower-like CuO/ZnO hybrid hierarchical nanostructures grown on copper substrate: Glycothermal synthesis, characterization, hydrophobic and anticorrosion properties. Materials (Basel). 10. https://doi.org/10.3390/ma10070697.

Bharat, T.C., Shubham, Mondal, S., Gupta, H.S., Singh, P.K., Das, A.K., 2019. Synthesis of doped zinc oxide nanoparticles: A review. Mater. Today Proc. 11, 767–775. https://doi.org/10.1016/j.matpr.2019.03.041

Bhardwaj, R., Pal, J., Hwa, K., Goyal, N., Gautam, S., 2018. Electronic and magnetic structure investigation of vanadium doped ZnO nanostructure. Vacuum 158, 257–262. https://doi.org/10.1016/j.vacuum.2018.09.053.

Bidier, S.A., Bououdina, M.R.H.M., 2017. Structural and optical characteristics of Ti-doped ZnO nanorods deposited by simple chemical bath deposition. J. Mater. Sci. Mater. Electron. 28, 11178–11185. https://doi.org/10.1007/s10854-017-6905-7.

Bidier, S.A., Hashim, M.R., Al-Diabat, A.M., Bououdina, M., 2017. Effect of growth time on Ti-doped ZnO nanorods prepared by low-temperature chemical bath deposition. Phys. E Low-Dimensional Syst. Nanostructures 88, 169–173. https://doi.org/10.1016/j.physe.2017.01.009.

Bousslama, W., Elhouichet, H., Férid, M., 2017. Optik Enhanced photocatalytic activity of Fe doped ZnO nanocrystals under sunlight irradiation. Opt. - Int. J. Light Electron Opt. 134, 88–98. https://doi.org/10.1016/j.ijleo.2017.01.025.

Byrappa, K., Yoshimura, M., 1992. Bonding Amalgam to Tooth Structure: A Scanning Electron Microscope Study, Journal of Esthetic and Restorative Dentistry. NOYES PUBLICATIONS, New Jersey. https://doi.org/10.1111/j.1708-8240.1992.tb00697.x

Caglar, Y., 2013. Sol-gel derived nanostructure undoped and cobalt doped ZnO: Structural, optical and electrical studies. J. Alloys Compd. 560, 181–188. https://doi.org/10.1016/j.jallcom.2013.01.080.

Cao, D., Gong, S., Shu, X., Zhu, D., Liang, S., 2019. Preparation of ZnO Nanoparticles with High Dispersibility Based on Oriented Attachment (OA) Process. Nanoscale Res. Lett. 14, 1–11. https://doi.org/https://doi.org/10.1186/s11671-019-3038-3

Carofiglio, M., Barui, S., Cauda, V., Laurenti, M., 2020. Doped zinc oxide nanoparticles: Synthesis, characterization and potential use in nanomedicine. Appl. Sci. 10. https://doi.org/10.3390/app10155194.

Chavillon, B., Cario, L., Renaud, A., Tessier, F., Cheviré, F., Boujtita, M., Pellegrin, Y., Blart, E., Smeigh, A., Hammarström, L., Odobel, F., Jobic, S., 2012. P-type nitrogen-doped ZnO nanoparticles stable under ambient conditions. J. Am. Chem. Soc. 134, 464–470. https://doi.org/10.1021/ja208044k.

Chen, J., Chen, D., He, J., Zhang, S., Chen, Z., 2009. The microstructure, optical, and electrical properties of sol-gel-derived Sc-doped and Al-Sc co-doped ZnO thin films. Appl. Surf. Sci. 255, 9413–9419. https://doi.org/10.1016/j.apsusc.2009.07.044.

Chen, J., Xiong, Y., Duan, M., Li, X., Li, J., Fang, S., Qin, S., Zhang, R., 2020. Insight into the Synergistic Effect of Adsorption-Photocatalysis for the Removal of Organic Dye Pollutants by Cr-Doped ZnO. Langmuir 36, 520–533. https://doi.org/10.1021/acs.langmuir.9b02879.

Chen, X., Shen, S., Guo, L., Mao, S.S., 2010. Semiconductor-based photocatalytic hydrogen generation. Chem. Rev. 110, 6503–6570. https://doi.org/10.1021/cr1001645.

Cherifi, Y., Chaouchi, A., Lorgoilloux, Y., Rguiti, M., Kadri, A., Courtois, C., 2016. Electrical, dielectric and photocatalytic properties of Fe-doped ZnO nanomaterials synthesized by sol gel method. Process. Appl. Ceram. 10, 125–135. https://doi.org/10.2298/PAC1603125C.

Chithra, M.J., Pushpanathan, K., Loganathan, M., 2014. Structural and Optical Properties of Co-Doped ZnO Nanoparticles Synthesized by Precipitation Method Structural and Optical Properties of Co-Doped ZnO Nanoparticles Synthesized by Precipitation Method. Mater. Manuf. Process. 29, 771–779. https://doi.org/10.1080/10426914.2014.892969.

Ciciliati, M.A., Silva, M.F., Fernandes, D.M., Melo, M.A.C. De, Adelina, A., Hechenleitner, W., Pineda, E.A.G., 2015. Fe-doped ZnO nanoparticles : Synthesis by a modified sol-gel method and characterization. Mater. Lett. 159, 84–86. https://doi.org/10.1016/j.matlet.2015.06.023.

Darmadi, I., Taufik, A., Saleh, R., 2020. Analysis of optical and structural properties of Ti-doped ZnO nanoparticles synthesized by co-precipitation method. J. Phys. Conf. Ser. 1442. https://doi.org/10.1088/1742-6596/1442/1/012021.

Das, A., Wary, R.R., Nair, R.G., 2020. Mn-doped ZnO: Role of morphological evolution on enhanced photocatalytic performance. Energy Reports 6, 737–741. https://doi.org/10.1016/j.egyr.2019.11.148.

Das, V.M., 2015. Red shift and Blue shift – By Virtue of B-Bit (YIN - Mass reality) Property of photons and it is Divine Mechanics (CCP, Code PcPs and CP) that controls Type of shift. IOSR. J. Res. Method Educ. Ver. II 5, 2320–7388. https://doi.org/10.9790/7388-056277101.

Debnath, T., Bandyopadhyay, A., Chakraborty, T., Das, S., 2019. Influence of different Cr concentrations on the structural and ferromagnetic properties of ZnO nanomaterials prepared by the hydrothermal synthesis route. Mater. Res. Bull. 118,. https://doi.org/10.1016/j.materresbull.2019.05.005 110480.

Deng, H., Fei, X., Yang, Y., Fan, J., Yu, J., Cheng, B., Zhang, L., 2021. S-scheme heterojunction based on p-type ZnMn2O4 and n-type ZnO with improved photocatalytic CO2 reduction activity. Chem. Eng. J. 409,. https://doi.org/10.1016/j.cej.2020.127377 127377.

Devi, P.G., Velu, A.S., 2016. Synthesis, structural and optical properties of pure ZnO and Co doped ZnO nanoparticles prepared by the co-precipitation method. J. Theor. Appl. Phys. 10, 233–240. https://doi.org/10.1007/s40094-016-0221-0.

Dixon, S.C., Sathasivam, S., Williamson, B.A., Scanlon, D.O., Carmalt, C.J., Parkin, I.P., 2017. Transparrent conducting n-type ZnO: Sc - synthesis, optoelectronic properties and theoretical insight †. J. Mater. Chem. C. https://doi.org/10.1039/C7TC02389H.

Djaja, N.F., Noorhidayati, A., Saleh, R., 2016. Synthesis, physical properties and catalytic activity of Cr-doped ZnO nanoparticles. AIP Conf. Proc. 1719. https://doi.org/10.1063/1.4943723.

Djaja, N.F., Taufik, A., Saleh, R., 2020. Synthesized vanadium doped ZnO through the co-precipitation method. J. Phys. Conf. Ser. 1442. https://doi.org/10.1088/1742-6596/1442/1/012023.

El-Ghoul, J., Kraini, M., El-Mir, L., 2015. Synthesis of Co-doped ZnO nanoparticles by sol–gel method and its characterization. J. Mater. Sci. Mater. Electron. 26, 2555–2562. https://doi.org/10.1007/s10854-015-2722-z.

Elilarassi, R., Chandrasekaran, G., 2011. Synthesis, structural and optical characterization of Ni-doped ZnO nanoparticles. J. Mater. Sci. Mater. Electron. 22, 751–756. https://doi.org/10.1007/s10854-010-0206-8.

Fabbiyola, S., Sailaja, V., Kennedy, L.J., Bououdina, M., Vijaya, J.J., 2017. Optical and magnetic properties of Ni-doped ZnO nanoparticles. J. Alloys Compd. 694, 522–531. https://doi.org/10.1016/j.jallcom.2016.10.022.

Fan, Q., Li, D., Li, J., Wang, C., 2020. Structure and piezoelectricity properties of V-doped ZnO thin films fabricated by sol-gel method. J. Alloys Compd. 829,. https://doi.org/10.1016/j.jallcom.2020.154483 154483.

Gahlawat, S., Singh, J., Yadav, A.K., Ingole, P.P., 2019. Exploring Burstein-Moss type effects in nickel doped hematite dendrite nanostructures for enhanced photo-electrochemical water splitting. Phys. Chem. Chem. Phys. 21, 20463–20477. https://doi.org/10.1039/c9cp04132j.

Gao, Q., Dai, Y., Li, C., Yang, L., Li, X., Cui, C., 2016. Correlation between oxygen vacancies and dopant concentration in Mn-doped ZnO nanoparticles synthesized by co-precipitation technique. J. Alloys Compd. 684, 669–676. https://doi.org/10.1016/j.jallcom.2016.05.227.

Gazzali, P.M.M., Rajan, S., Chandrasekaran, G., 2018. Low-Temperature Magnetic Properties of Vanadium-Doped ZnO Nanoparticles. J. Supercond. Nov. Magn. 31, 2817–2828. https://doi.org/10.1007/s10948-017-4537-z.

Ge, Z., Wang, C., Chen, T., Chen, Z., Wang, T., Guo, L., Qi, G., Liu, J., 2021. Preparation of Cu-doped ZnO nanoparticles via layered double hydroxide and application for dye-sensitized solar cells. J. Phys. Chem. Solids 150,. https://doi.org/10.1016/j.jpcs.2020.109833 109833.

Ghahramanifard, F., Rouhollahi, A., Fazlolahzadeh, O., 2018. Electrodeposition of Cu-doped p-type ZnO nanorods; effect of Cu doping on structural, optical and photoelectrocatalytic property of ZnO nanostructure. Superlattices Microstruct. 114, 1–14. https://doi.org/10.1016/j.spmi.2017.07.019.

Ghoul, J. El, 2016. Synthesis of vanadium doped ZnO nanoparticles by sol-gel method and its characterization. J. Mater. Sci. Mater. Electron. 27, 2159–2165. https://doi.org/10.1007/s10854-015-4006-z.

Gnanamozhi, P., Renganathan, V., Chen, S.M., Pandiyan, V., Antony Arockiaraj, M., Alharbi, N.S., Kadaikunnan, S., Khaled, J.M., Alanzi, K.F., 2020. Influence of Nickel concentration on the photocatalytic dye degradation (methylene blue and reactive red 120) and antibacterial activity of ZnO nanoparticles. Ceram. Int. 46, 18322–18330. https://doi.org/10.1016/j.ceramint.2020.05.054.

Grabianska, K., Kucharski, R., Puchalski, A., Sochacki, T., Bockowski, M., 2020. Recent progress in basic ammonothermal GaN crystal growth. J. Cryst. Growth 547,. https://doi.org/10.1016/j.jcrysgro.2020.125804 125804.

Habba, Y.G., Capochichi-gnambodoe, M., Leprince-wang, Y., 2017. Enhanced Photocatalytic Activity of Iron-Doped ZnO Nanowires for Water Purification. Appl. Sci. 7, 1–10. https://doi.org/10.3390/app7111185.

Han, C., Duan, L., Zhao, X., Hu, Z., Niu, Y., Geng, W., 2019. Effect of Fe doping on structural and optical properties of ZnO films and nanorods. J. Alloys Compd. 770, 854–863. https://doi.org/10.1016/j.jallcom.2018.08.217.

Hanh, N.T., Le Minh Tri, N., Van Thuan, D., Thanh Tung, M.H., Pham, T.D., Minh, T.D., Trang, H.T., Binh, M.T., Nguyen, M.V., 2019. Monocrotophos pesticide effectively removed by novel visible light driven Cu doped ZnO photocatalyst. J. Photochem. Photo-

biol. A Chem. 382,. https://doi.org/10.1016/j.jphotochem.2019.111923 111923.

Haq, K., Irfan, M., Masood, M., Saleem, M., Iqbal, T., Ahmad, I., Khan, M., Zaffar, M., Irfan, Muhammad, 2018. Enhanced room temperature ferromagnetism in Cr-doped ZnO nanoparticles prepared by auto-combustion method. J. Semicond. 39,. https://doi.org/10.1088/1674-4926/39/4/043001 043001.

Hassan, M.M., Khan, W., Azam, A., Naqvi, A.H., 2015. Influence of Cr incorporation on structural, dielectric and optical properties of ZnO nanoparticles. J. Ind. Eng. Chem. 21, 283–291. https://doi.org/10.1016/j.jiec.2014.01.047.

Hui, A., Ma, J., Liu, J., Bao, Y., Zhang, J., 2017. Morphological evolution of Fe doped sea urchin-shaped ZnO nanoparticles with enhanced photocatalytic activity. J. Alloys Compd. 696, 639–647. https://doi.org/10.1016/j.jallcom.2016.10.319.

Iqbal, J., Safdar, N., Jan, T., Ismail, M., Hussain, S.S., Mahmood, A., Shahzad, S., Mansoor, Q., 2015. Journal of Materials Science & Technology Facile Synthesis as well as Structural, Raman, Dielectric and Antibacterial Characteristics of Cu Doped ZnO Nanoparticles. J. Mater. Sci. Technol. 31, 300–304. https://doi.org/10.1016/j.jmst.2014.06.013.

Iqbal, M., Thebo, A.A., Jatoi, W.B., Tabassum, M.T., Rehman, M. U., Thebo, K.H., Mohsin, M.A., Ullah, S., Jatoi, A.H., Shah, I., 2020. Facile synthesis of Cr doped hierarchical ZnO nano-structures for enhanced photovoltaic performance. Inorg. Chem. Commun. 116,. https://doi.org/10.1016/j.inoche.2020.107902 107902.

Jellal, I., Nouneh, K., Toura, H., Boutamart, M., Briche, S., Naja, J., Soucase, B.M., Touhami, M.E., 2021. Enhanced photocatalytic activity of supported Cu-doped ZnO nanostructures prepared by SILAR method. Opt. Mater. Amst). 111,. https://doi.org/10.1016/j.optmat.2020.110669 110669.

Jiang, X., Zhang, B., Liu, B., Tang, X., Tang, L., 2019. Experimental and theoretical study of visible light driven scandium (III) doped ZnO for antibacterial activity. Ceram. Int. 45, 19948–19955. https://doi.org/10.1016/j.ceramint.2019.06.252.

Jongnavakit, P., Amornpitoksuk, P., Suwanboon, S., Ndiege, N., 2012. Preparation and photocatalytic activity of Cu-doped ZnO thin films prepared by the sol-gel method. Appl. Surf. Sci. 258, 8192–8198. https://doi.org/10.1016/j.apsusc.2012.05.021.

Kadam, A.N., Gon, T., Su, D., Garadkar, K.M., Park, J., 2017. Morphological evolution of Cu doped ZnO for enhancement of photocatalytic activity. J. Alloys Compd. 710, 102–113. https://doi.org/10.1016/j.jallcom.2017.03.150.

Kalita, A., Kalita, M.P.C., 2019. Microstructural, optical, magnetic and photocatalytic properties of Mn doped ZnO nanocrystals of different sizes. Phys. B Condens. Matter 552, 30–46. https://doi.org/10.1016/j.physb.2018.08.028.

Kanchana, S., Chithra, M.J., Ernest, S., Pushpanathan, K., 2016. Violet emission from Fe doped ZnO nanoparticles synthesized by precipitation method. J. Lumin. 176, 6–14. https://doi.org/10.1016/j.jlumin.2015.12.047.

Kaphle, A., Reed, T., Apblett, A., Hari, P., 2019. Doping efficiency in cobalt-doped ZnO nanostructured materials. J. Nanomater. 2019. https://doi.org/10.1155/2019/7034620.

Kaur, P., Rahul, Kaur, S., Kriti, Arora, D., Asokan, K., Paul Singh, D., 2019. Correlation between lattice deformations and optical properties of Ni doped ZnO at dilute concentration. Mater. Today Proc. 26, 3436–3441. https://doi.org/10.1016/j.matpr.2019.12.001

Kayani, Z.N., Abbas, E., Saddiqe, Z., Riaz, S., Naseem, S., 2018. Photocatalytic, antibacterial, optical and magnetic properties of Fe-doped ZnO nano-particles prepared by sol-gel. Mater. Sci. Semicond. Process. 88, 109–119. https://doi.org/10.1016/j.mssp.2018.08.003.

Kayani, Z.N., Anjum, M., Riaz, S., Naseem, S., Zeeshan, T., 2020. Role of Mn in biological, optical, and magnetic properties ZnO nano-particles. Appl. Phys. A Mater. Sci. Process. 126. https://doi.org/10.1007/s00339-020-3380-4.

Khan, H., Habib, M., Khan, A., Boffito, D.C., 2020. A modified sol-gel synthesis to yield a stable Fe3 + /ZnO photocatalyst: Degradation of water pollutants and mechanistic insights under UV and visible light. J. Environ. Chem. Eng. 8,. https://doi.org/10.1016/j.jece.2020.104282 104282.

Khan, Ibrahim, Saeed, K., Khan, Idrees, 2019. Nanoparticles: Properties, applications and toxicities. Arab. J. Chem. 12, 908–931. https://doi.org/10.1016/j.arabjc.2017.05.011.

Khan, M.A.M., Kumar, S., Alhazaa, A.N., Al-gawati, M.A., 2018. Modifications in structural, morphological, optical and photocatalytic properties of ZnO: Mn nanoparticles by sol-gel protocol. Mater. Sci. Semicond. Process. 87, 134–141. https://doi.org/10.1016/j.mssp.2018.07.016.

Khodadadi, B., Bordbar, M., Yeganeh-Faal, A., 2016. Optical, structural, and photocatalytic properties of Cd-doped ZnO powders prepared via sol-gel method. J. Sol-Gel Sci. Technol. 77, 521–527. https://doi.org/10.1007/s10971-015-3877-z.

Kim, D., Kim, W., Jeon, S., Yong, K., 2017. Highly efficient UV-sensing properties of Sb-doped ZnO nanorod arrays synthesized by a facile, single-step hydrothermal reaction. RSC Adv. 7, 40539–40548. https://doi.org/10.1039/C7RA07157D.

Klett, C., Barry, A., Balti, I., Lelli, P., Schoenstein, F., Jouini, N., 2014. Nickel doped Zinc oxide as a potential sorbent for decolorization of specific dyes, methylorange and tartrazine by adsorption process. J. Environ. Chem. Eng. 2, 914–926. https://doi.org/10.1016/j.jece.2014.03.001.

Kominami, H., Miyakawa, M., Murakami, S., Yasuda, T., Kohno, M., Onoue, S., Kera, Y., Ohtani, B., 2001. Solvothermal synthesis of tantalum (V) oxide nanoparticles and their photocatalytic activities in aqueous suspension systems. Phys. Chem. Chem. Phys. 3, 2697–2703. https://doi.org/https://doi.org/10.1039/B101313K

Korir, K.K., Benecha, E.M., Nyamwala, F.O., Lombardi, E.B., 2021. Tuning electronic structure of ZnO nanowires via 3d transition metal dopants for improved photo-electrochemical water splitting: An ab initio study. Mater. Today Commun. 26,. https://doi.org/10.1016/j.mtcomm.2020.101929 101929.

Kumar, K., Chitkara, M., Singh, I., Mehta, D., Kumar, S., 2014. Photocatalytic, optical and magnetic properties of Fe-doped ZnO nanoparticles prepared by chemical route. J. Alloys Compd. 588, 681–689. https://doi.org/10.1016/j.jallcom.2013.11.127.

Kumar, M., Arjmand, M., Sundararaj, U., 2018. Ultrasonics-Sonochemistry Ultrasound-assisted synthesis and characterization of magnetite nanoparticles and poly (methyl methacrylate)/ magnetite nanocomposites. Ultrason. - Sonochemistry 43, 38–51. https://doi.org/10.1016/j.ultsonch.2017.12.035.

Kumari, P., Misra, K.P., Chattopadhyay, S., Samanta, S., 2021. A brief review on transition metal ion doped ZnO nanoparticles and its optoelectronic applications. Mater. Today Proc. https://doi.org/10.1016/j.matpr.2021.02.299

Labhane, P.K., Huse, V.R., Patle, L.B., Chaudhari, A.L., Sonawane, G.H., 2015. Synthesis of Cu Doped ZnO Nanoparticles: Crystallographic, Optical, FTIR, Morphological and Photocatalytic Study. J. Mater. Sci. Chem. Eng. 3, 39–51. https://doi.org/10.4236/msce.2015.37005

Li, B.S., Xiao, Z.Y., Ma, J.G., Liu, Y.C., 2017a. The p-type ZnO thin films obtained by a reversed substitution doping method of thermal oxidation of Zn3N2 precursors. Chinese Phys. B 26, 1–14. https://doi.org/10.1088/1674-1056/26/11/117101.

Li, W., Wang, G., Chen, C., Liao, J., Li, Z., 2017b. Enhanced Visible Light Photocatalytic Activity of ZnO Nanowires Doped with Mn2 + and Co2 + Ions. Nanomaterials 7, 1–11. https://doi.org/10.3390/nano7010020.

Liau, L.C., Huang, J., 2017. Energy-level variations of Cu-doped ZnO fabricated through sol-gel processing. J. Alloys Compd. 702, 153–160. https://doi.org/10.1016/j.jallcom.2017.01.174.

Lima, M.K., Fernandes, D.M., Silva, M.F., Baesso, M.L., Neto, A. M., de Morais, G.R., Nakamura, C.V., de Oliveira Caleare, A., Hechenleitner, A.A.W., Pineda, E.A.G., 2014. Co-doped ZnO

nanoparticles synthesized by an adapted sol-gel method: Effects on the structural, optical, photocatalytic and antibacterial properties. J Sol-Gel Sci Technol 72, 301–309. https://doi.org/10.1007/s10971-014-3310-z.

Liu, X., Hu, M., Chu, X., 2013. Synthesis and field emission properties of highly ordered Ti-doped ZnO nanoarray structure. J Matter Sci Mater Electron 24, 2839–2845. https://doi.org/10.1007/s10854-013-1180-8.

Loyola Poul Raj, I., Jegatha Christy, A., David Prabu, R., Chidhambaram, N., Shkir, M., AlFaify, S., Khan, A., 2020. Significance of Ni doping on structure-morphology-photoluminescence, optical and photocatalytic activity of CBD grown ZnO nanowires for opto-photocatalyst applications. Inorg. Chem. Commun. 119, 108082. https://doi.org/10.1016/j.inoche.2020.108082

Luo, S., Yan, B., Shen, J., 2012. Enhancement of photoelectric and photocatalytic activities: Mo doped TiO2 thin films deposited by sputtering. Thin Solid Films 522, 361–365. https://doi.org/10.1016/j.tsf.2012.07.121.

Ma, Q., Lv, X., Wang, Y., Chen, J., 2016. Optical and photocatalytic properties of Mn doped flower-like ZnO hierarchical structures. Opt. Mater. (Amst) 60, 86–93. https://doi.org/10.1016/j.optmat.2016.07.014.

Ma, Q., Yang, X., Lv, X., Jia, H., Wang, Y., 2019. Cu doped ZnO hierarchical nanostructures: morphological evolution and photocatalytic property. J. Mater. Sci. Mater. Electron. 30, 2309–2315. https://doi.org/10.1007/s10854-018-0503-1.

Ma, Z., Ren, F., Deng, Y., Volinsky, A.A., 2020. Structural, electrochemical and optical properties of Ni doped ZnO: Experimental and theoretical investigation. Optik (Stuttg). 219,. https://doi.org/10.1016/j.ijleo.2020.165204 165204.

Mahdavi, R., Talesh, S.S.A., 2017. Sol-gel synthesis, structural and enhanced photocatalytic performance of Al doped ZnO nanoparticles. Adv. Powder Technol. 28, 1418–1425. https://doi.org/10.1016/j.apt.2017.03.014.

Mahmood, A., Naeem, A., 2017. Sol-Gel-Derived Doped ZnO Thin Films: Processing, World's largest Science, Technology & Medicine Open Access book publisher. Intech Open Sci. Open minds. https://doi.org/10.5772/67857

Margan, P., Haghighi, M., 2018. Ultrasonics-Sonochemistry Sonocoprecipitation synthesis and physicochemical characterization of CdO-ZnO nanophotocatalyst for removal of acid orange 7 from wastewater. Ultrason. - Sonochemistry 40, 323–332. https://doi.org/10.1016/j.ultsonch.2017.07.003

Mazurek, A.H., Szeleszczuk, Ł., Pisklak, D.M., 2020. Periodic DFT calculations—Review of applications in the pharmaceutical sciences. Pharmaceutics 12. https://doi.org/10.3390/pharmaceutics12050415.

Meng, A., Xing, J., Li, X., Yang, L., Li, Z., 2019. Cr(III)-doped ZnO nanoflowers: synthesis, mechanism and enhanced photocatalytic activity. J. Nanosci. Nanotechnol. 19, 2617–2624. https://doi.org/10.1166/jnn.2019.15812.

Miao, C., Zhao, Z., Ma, X., Ma, Z., 2010. Studies on the properties of sputter-deposited Sc-doped ZnO thin film. Phys. B Condens. Matter 405, 3787–3790. https://doi.org/10.1016/j.physb.2010.05.087.

Mishra, A.K., Das, D., 2010. Investigation on Fe-doped ZnO nanostructures prepared by a chemical route. Mater. Sci. Eng. B 171, 5–10. https://doi.org/10.1016/j.mseb.2010.03.045.

Modwi, A., Abbo, M.A., Houas, E.A.H.A., 2016. Effect of annealing on physicochemical and photocatalytic activity of Cu 5 % loading on ZnO synthesized by sol-gel method. J. Mater. Sci. Mater. Electron. 27, 12974–12984. https://doi.org/10.1007/s10854-016-5436-y.

Mondal, A., Giri, N., Sarkar, S., Majumdar, S., Ray, R., 2019. Materials Science in Semiconductor Processing Tuning the photocatalytic activity of ZnO by TM (TM = Fe Co, Ni) doping. Mater. Sci. Semicond. Process. 91, 333–340. https://doi.org/10.1016/j.mssp.2018.12.003.

Mote, V.D., Purushotham, Y., Dole, B.N., 2016. Structural, morphological, physical and dielectric properties of Mn doped ZnO nanocrystals synthesized by sol-gel method. Mater. Des. 96, 99–105. https://doi.org/10.1016/j.matdes.2016.02.016.

Motelica, L., Marinof, L., Holban, A., Vasile, B.S., Ficai, A., 2020a. Optical, photocatalytic and antibacterial properties of zinc oxide nanoparticles obtained by a Solvothermal method. UPB Sci. Bull. Ser. B Chem. Mater. Sci. 82, 59–70.

Motelica, L., Popescu, A., Răzvan, A.G., Oprea, O., Truşcă, R.D., Vasile, B.S., Dumitru, F., Holban, A.M., 2020b. Facile use of zno nanopowders to protect old manual paper documents. Materials (Basel). 13, 1–20. https://doi.org/10.3390/ma13235452.

Muñoz-Aguirre, N., Martínez-Pérez, L., Muñoz-Aguirre, S., Flores-Herrera, L.A., Hernández, E.V., Zelaya-Angel, O., 2019. Luminescent properties of (004) highly oriented cubic zinc blende ZnO thin films. Materials (Basel). 12, 1–10. https://doi.org/10.3390/ma12203314.

Muthukumar, T., Shenbagapushpam, M., Madasamy, S.B., Paulpandian, M.M., Kodirajan, S., 2020. Fabrication of hard bound mesoporous silica stabilized Cu(I) electrocatalyst for 4-nitrophenol sensor via alcothermal strategy. J. Electroanal. Chem. 859,. https://doi.org/10.1016/j.jelechem.2019.113792 113792.

Naeem, M., Qaseem, S., Gul, I.H., Maqsood, A., 2010. Study of active surface defects in Ti doped ZnO nanoparticles Study of active surface defects in Ti doped ZnO nanoparticles. J. Appl. Phys. 107. https://doi.org/10.1063/1.3432571.

Narayanan, N., Deepak, N.K., 2018. Optik Enhancement of visible luminescence and photocatalytic activity of ZnO thin films via Cu doping. Opt. - Int. J. Light Electron Opt. 158, 1313–1326. https://doi.org/10.1016/j.ijleo.2018.01.024.

Naz, F., Saeed, K., 2021. Investigation of photocatalytic behavior of undoped ZnO and Cr-doped ZnO nanoparticles for the degradation of dye. Inorg. Nano-Metal Chem. 51, 1–11. https://doi.org/10.1080/24701556.2020.1749657.

Ng, Z.N., Chan, K.Y., Muslimin, S., Knipp, D., 2018. P-Type Characteristic of Nitrogen-Doped ZnO Films. J. Electron. Mater. 47, 5607–5613. https://doi.org/10.1007/s11664-018-6468-2.

Nguyen, S.N., Truong, T.K., You, S., Wang, Y., Cao, T.M., Pham, V. Van, 2019. Investigation on Photocatalytic Removal of NO under Visible Light over Cr-Doped ZnO Nanoparticles. ACS Omega 4, 12853–12859. https://doi.org/10.1021/acsomega.9b01628.

Nithya, R., Ragupathy, S., Sakthi, D., Arun, V., Kannadasan, N., 2020. A study on Mn doped ZnO loaded on CSAC for the photocatalytic degradation of brilliant green dye. Chem. Phys. Lett. 755,. https://doi.org/10.1016/j.cplett.2020.137769 137769.

Nurfani, E., Lailani, A., Kesuma, W.A.P., Anrokhi, M.S., Kadja, G.T.M., Rozana, M., 2021. UV sensitivity enhancement in Fe-doped ZnO films grown by ultrafast spray pyrolysis. Opt. Mater. Amst). 112,. https://doi.org/10.1016/j.optmat.2020.110768 110768.

Ong, C.B., Mohammad, A.W., Ng, L.Y., 2019. Integrated adsorption-solar photocatalytic membrane reactor for degradation of hazardous Congo red using Fe-doped ZnO and Fe-doped ZnO/rGO nanocomposites. Environ. Sci. Pollut. Res. 26, 33856–33869. https://doi.org/10.1007/s11356-018-2557-2.

Ong, C.B., Ng, L.Y., Mohammad, A.W., 2018. A review of ZnO nanoparticles as solar photocatalysts: Synthesis, mechanisms and applications. Renew. Sustain. Energy Rev. 81, 536–551. https://doi.org/10.1016/j.rser.2017.08.020.

Pan, H., Zhang, Y., Hu, Y., Xie, H., 2020. Effect of cobalt doping on optical, magnetic and photocatalytic properties of ZnO nanoparticles. Optik (Stuttg). 208. https://doi.org/10.1016/j.ijleo.2020.164560.

Pascariu, P., Tudose, I.V., Suchea, M., Koudoumas, E., Fifere, N., Airinei, A., 2018. Preparation and characterization of Ni, Co doped ZnO nanoparticles for photocatalytic applications. Appl. Surf. Sci. 448, 481–488. https://doi.org/10.1016/j.apsusc.2018.04.124.

Pimentel, A., Ferreira, S.H., Nunes, D., Calmeiro, T., Martins, R., Fortunato, E., 2016. Microwave synthesized ZnO nanorod arrays for UV sensors: A seed layer annealing temperature study. Materials (Basel). 9, 1–15. https://doi.org/10.3390/ma9040299.

Poongodi, G., Anandan, P., Kumar, R.M., Jayavel, R., 2015. Studies on visible light photocatalytic and antibacterial activities of nanostructured cobalt doped ZnO thin films prepared by sol-gel spin coating method. Spectrochim. Acta - Part A Mol. Biomol. Spectrosc. 148, 237–243. https://doi.org/10.1016/j.saa.2015.03.134.

Poornaprakash, B., Chalapathi, U., Subramanyam, K., Vattikuti, S. V.P., Park, S.H., 2020. Wurtzite phase Co-doped ZnO nanorods: Morphological, structural, optical, magnetic, and enhanced photocatalytic characteristics. Ceram. Int. 46, 2931–2939. https://doi.org/10.1016/j.ceramint.2019.09.289.

Prerna, Arya, S., Sharma, A., Singh, B., Tomar, A., Singh, S., Sharma, R., 2020. Morphological and Optical Characterization of Sol-Gel Synthesized Ni-Doped ZnO Nanoparticles. Integr. Ferroelectr. 205, 1–13. https://doi.org/10.1080/10584587.2019.1674992

Putri, N.A., Fauzia, V., Iwan, S., Roza, L., Ali, A., Budi, S., 2018. Mn-doping-induced photocatalytic activity enhancement of ZnO nanorods prepared on glass substrates. Appl. Surf. Sci. 439, 285–297. https://doi.org/10.1016/j.apsusc.2017.12.246.

Qi, K., Cheng, B., Yu, J., Ho, W., 2017. Review on the improvement of the photocatalytic and antibacterial activities of ZnO. J. Alloys Compd. 727, 792–820. https://doi.org/10.1016/j.jallcom.2017.08.142.

Raebiger, H., Lany, S., Zunger, A., 2009. Electronic structure, donor and acceptor transitions, and magnetism of 3d impurities in In2 O3 and ZnO. Phys. Rev. B - Condens. Matter Mater. Phys. 79, 1–7. https://doi.org/10.1103/PhysRevB.79.165202.

Rahman, M.U., Wei, M., Xie, F., Khan, M., 2019. Efficient dye-sensitized solar cells composed of nanostructural zno doped with ti. Catalysts 9, 1–11. https://doi.org/10.3390/catal9030273.

Raja, K., Ramesh, P.S., Geetha, D., 2014. Synthesis, structural and optical properties of ZnO and Ni-doped ZnO hexagonal nanorods by Co-precipitation method. Spectrochim. Acta - Part A Mol. Biomol. Spectrosc. 120, 19–24. https://doi.org/10.1016/j.saa.2013.09.103.

Rajasekaran, M., Arunachalam, A., Kumaresan, P., 2020. Structural, morphological and optical characterization of Ti-doped ZnO nanorod thin film synthesized by spray pyrolysis technique. Mater. Res. Express 7. https://doi.org/10.1088/2053-1591/ab815d.

Rajivgandhi, G.N., Ramachandran, G., Alharbi, N.S., Kadaikunnan, S., Khaleed, J.M., Manokaran, N., Li, W.J., 2021. Substantial effect of Cr doping on the antimicrobial activity of ZnO nanoparticles prepared by ultrasonication process. Mater. Sci. Eng. B Solid-State Mater. Adv. Technol. 263,. https://doi.org/10.1016/j.mseb.2020.114817 114817.

Ramadan, R., Romera, D., Carraascon, R.D., Cantero, M., Aguilera-Correa, J.-J., Ruiz, J.P.G., Esteban, J., Silvan, M.M., 2019. Sol-Gel-Deposited Ti-Doped ZnO : Toward Cell Fouling Transparent Conductive Oxides. ACS Omega 4, 11354–11363. https://doi.org/10.1021/acsomega.9b00646.

Ramany, K., Shankararajan, R., Savarimuthu, K., Elumalai, P., Rajamanickam, G., Narendhiran, S., Perumalsamy, R., 2019. Comparative study on hydrothermally synthesized undoped and Vanadium doped Zinc Oxide nanorods for nanoelectromechanical systems low- frequency accelerometer application. Thin Solid Films 680, 60–66. https://doi.org/10.1016/j.tsf.2019.04.018.

Rana, S.B., Singh, R.P.P., 2016. Investigation of structural, optical, magnetic properties and antibacterial activity of Ni-doped zinc oxide nanoparticles. J. Mater. Sci. Mater. Electron. 27, 9346–9355. https://doi.org/10.1007/s10854-016-4975-6.

Rao, K.S., Vanaja, T., 2015. Influence of Transition Metal (Cu, Al) ions Doping on Structural and Optical properties of ZnO Nanopowders. Mater. Today Proc. 2 (2), 3743–3749. https://doi.org/10.1016/j.matpr.2015.07.163.

Raskar, N.D., Dake, D.V., Mane, V.A., Stathatos, E., Deshpande, U., Dole, B., 2019. One step synthesis of vertically grown Mn-doped ZnO nanorods for photocatalytic application. J. Mater. Sci. Mater. Electron. 30, 10886–10899. https://doi.org/10.1007/s10854-019-01433-7.

Ray, R., Kumar, A., Paul, A.K., Tyagi, S., 2016. Enhanced Photocatalytic Performance of Chromium Doped Zinc Oxide Nanoparticles. Trans. Indian Inst. Met. 69, 1043–1048. https://doi.org/10.1007/s12666-015-0618-5.

Rodriguez-Gattorno, G., Oskam, G., 2006. Forced Hydrolysis vs Self-Hydrolysis of Zinc Acetate in Ethanol and Iso-butanol. ECS Trans. 3, 23–28. https://doi.org/10.1149/1.2357093.

Roguai, S., Djelloul, A., 2020. A structural and optical properties of Cu-doped ZnO films prepared by spray pyrolysis. Appl. Phys. A Mater. Sci. Process. 126, 1–8. https://doi.org/10.1007/s00339-020-3301-6.

Rooydell, R., Brahma, S., Wang, R., Roshanzamir, M., Ebrahimzadeh, F., Liu, C., 2017. Cu doped ZnO nanorods with controllable Cu content by using single metal organic precursors and their photocatalytic and luminescence properties. J. Alloys Compd. 691, 936–945. https://doi.org/10.1016/j.jallcom.2016.08.324.

Saadi, H., Rhouma, F.I.H., Benzarti, Z., Bougrioua, Z., Guermazi, S., Khirouni, K., 2020. Electrical conductivity improvement of Fe doped ZnO nanopowders. Mater. Res. Bull. 129,. https://doi.org/10.1016/j.materresbull.2020.110884 110884.

Safa, S., Mokhtari, S., Khayatian, A., Azimirad, R., 2018. Improving ultraviolet photodetection of ZnO nanorods by Cr doped ZnO encapsulation process. Opt. Commun. 413, 131–135. https://doi.org/10.1016/j.optcom.2017.12.038.

Sahal, M., Mollar, M., Mari, B., 2016. p-and n-type Doping of Zinc Oxide through Electrochemical Methods. 2016 Int. Renew. Sustain. Energy Conf. 11–15. https://doi.org/10.1109/IRSEC.2016.7984057.

Saharan, P., Ram, G., Lata, S., Mehta, S.K., Mor, S., 2015. Ultra fast and effective treatment of dyes from water with the synergistic effect of Ni doped ZnO nanoparticles and ultrasonication. Ultrason. - Sonochemistry 22, 317–325. https://doi.org/10.1016/j.ultsonch.2014.07.004.

Sahu, J., Soni, S., Kumar, Sudhish, Dalela, B., Alvi, P.A., Sharma, S. S., Phase, D.M., Gupta, M., Kumar, Shalendra, Dalela, S., 2020. Defects and oxygen vacancies tailored structural, optical and electronic structure properties of Co-doped ZnO nanoparticle samples probed using soft X-ray absorption spectroscopy. Vacuum 179,. https://doi.org/10.1016/j.vacuum.2020.109538 109538.

Sajjad, M., Ullah, I., Khan, M.I., Khan, J., Khan, M.Y., Tauseef, M., 2018. Structural and optical properties of pure and copper doped zinc oxide nanoparticles. Results Phys. 9, 1301–1309. https://doi.org/10.1016/j.rinp.2018.04.010.

Salah, N., Hameed, A., Aslam, M., Babkair, S.S., Bahabri, F.S., 2016. Photocatalytic activity of V doped ZnO nanoparticles thin films for the removal of 2-chlorophenol from the aquatic environment under natural sunlight exposure. J. Environ. Manage. 177, 53–64. https://doi.org/10.1016/j.jenvman.2016.04.007.

Samadi, M., Zirak, M., Naseri, A., Khorashadizade, E., Moshfegh, A.Z., 2016. Recent progress on doped ZnO nanostructures for visible-light photocatalysis. Thin Solid Films 605, 2–19. https://doi.org/10.1016/j.tsf.2015.12.064.

Shah, A.A., Bhatti, M.A., Tahira, A., Chandio, A.D., Channa, I.A., Sahito, A.G., Chalangar, E., Willander, M., Nur, O., Ibupoto, Z. H., 2020. Facile synthesis of copper doped ZnO nanorods for the efficient photo degradation of methylene blue and methyl orange. Ceram. Int. 46, 9997–10005. https://doi.org/10.1016/j.ceramint.2019.12.024.

Sharma, D.K., Shukla, S., Sharma, K.K., Kumar, V., 2020. A review on ZnO: Fundamental properties and applications. Mater. Today Proc. https://doi.org/10.1016/j.matpr.2020.10.238

Sharma, R., Sehrawat, K., Wakahara, A., Mehra, R.M., 2009. Epitaxial growth of Sc-doped ZnO films on Si by sol-gel route.

Appl. Surf. Sci. 255, 5781–5788. https://doi.org/10.1016/j.apsusc.2009.01.004

Shayegan, Z., Lee, C., Haghighat, F., 2018. TiO 2 photocatalyst for removal of volatile organic compounds in gas phase – A review. Chem. Eng. J. 334, 2408–2439. https://doi.org/10.1016/j.cej.2017.09.153

Shohany, B.G., Zak, A.K., 2020. Doped ZnO nanostructures with selected elements - Structural, morphology and optical properties: A review. Ceram. Int. 46, 5507–5520. https://doi.org/10.1016/j.ceramint.2019.11.051.

Singh, J., Rathi, A., Rawat, M., Kumar, V., Kim, K., 2019a. The effect of manganese doping on structural, optical, and photocatalytic activity of zinc oxide nanoparticles. Compos. Part B 166, 361–370. https://doi.org/10.1016/j.compositesb.2018.12.006.

Singh, P., Kumar, R., Singh, R.K., 2019b. Progress on Transition Metal-Doped ZnO Nanoparticles and Its Application. Ind. Eng. Chem. Res. 58, 17130–17163. https://doi.org/10.1021/acs.iecr.9b01561.

Slama, R., El Ghoul, J., Ghiloufi, I., Omri, K., El Mir, L., Houas, A., 2016. Synthesis and physico-chemical studies of vanadium doped zinc oxide nanoparticles and its photocatalysis. J. Mater. Sci. Mater. Electron. 27, 8146–8153. https://doi.org/10.1007/s10854-016-4817-6.

Slama, R., Ghribi, F., Houas, A., Barthou, C., Mir, L. El, 2011. Visible photocatalytic properties of vanadium doped zinc oxide aerogel nanopowder. Thin Solid Films 519, 5792–5795. https://doi.org/10.1016/j.tsf.2010.12.197.

Smijs, T.G., Pavel, S., 2011. Titanium dioxide and zinc oxide nanoparticles in sunscreens: Focus on their safety and effectiveness. Nanotechnol. Sci. Appl. 4, 95–112. https://doi.org/10.2147/nsa.s19419.

Srinet, G., Sharma, S., Siqueiros, B.P.J.M., 2018. Investigations on the physical properties of Mn-modified ZnO samples prepared by sol-gel route. J. Mater. Sci. Mater. Electron. 29, 9930–9941. https://doi.org/10.1007/s10854-018-9035-y.

Srinivasulu, T., Saritha, K., Reddy, K.T.R., 2017. Synthesis and characterization of Fe-doped ZnO thin films deposited by chemical spray pyrolysis. Mod. Electron. Mater. 3, 76–85. https://doi.org/10.1016/j.moem.2017.07.001.

Šutka, A., Käämbre, T., Pärna, R., Juhnevica, I., Maiorov, M., Joost, U., Kisand, V., 2016. Co doped ZnO nanowires as visible light photocatalysts. Solid State Sci. 56, 54–62. https://doi.org/10.1016/j.solidstatesciences.2016.04.008.

Tahir, N., Hussain, S.T., Usman, M., Hasanain, S.K., Mumtaz, A., 2009. Effect of vanadium doping on structural, magnetic and optical properties of ZnO nanoparticles. Appl. Surf. Sci. 255, 8506–8510. https://doi.org/10.1016/j.apsusc.2009.06.003.

Tao, Y., 2016. Screen-printed front junction n-type silicon solar cells. Intech 13. https://doi.org/http://dx.doi.org/10.5772/63198

Thein, M.T., Pung, S., Aziz, A., Itoh, M., 2016. Journal of the Taiwan Institute of Chemical Engineers Effect of Ni coupling on the photoluminescence property and photocatalytic activity of ZnO nanorods. J. Taiwan Inst. Chem. Eng. 61, 156–165. https://doi.org/10.1016/j.jtice.2015.11.024.

Thennarasu, G., Sivasamy, A., 2016. Enhanced visible photocatalytic activity of cotton ball like nano structured Cu doped ZnO for the degradation of organic pollutant. Ecotoxicol. Environ. Saf. 134, 412–420. https://doi.org/10.1016/j.ecoenv.2015.10.030.

Ton-that, C., Foley, M., Phillips, M.R., Tsuzuki, T., Smith, Z., 2012. Correlation between the structural and optical properties of Mn-doped ZnO nanoparticles. J. Alloys Compd. 522, 114–117. https://doi.org/10.1016/j.jallcom.2012.01.116.

Toufiq, A.M., Hussain, R., Shah, A., Mahmood, A., Rehman, A., Khan, A., Rahman, S. ur, 2021. The influence of Mn doping on the structural and optical properties of ZnO nanostructures. Phys. B Condens. Matter 604, 412731. https://doi.org/10.1016/j.physb.2020.412731

Truong, T.K., Van Doan, T., Tran, H.H., Van Le, H., Lam, V.Q., Tran, H.N., Cao, T.M., Van Pham, V., 2019. Effect of Cr Doping on Visible-Light-Driven Photocatalytic Activity of ZnO Nanoparticles. J. Electron. Mater. 48, 7378–7388. https://doi.org/10.1007/s11664-019-07566-z.

Tseng, Y., Lin, Y., Chang, H., Chen, Y., Liu, C., Zou, Y., 2012. Effects of Ti content on the optical and structural properties of the Ti-doped ZnO nanoparticles. J. Lumin. 132, 491–494. https://doi.org/10.1016/j.jlumin.2011.08.016.

Turkyilmaz, S. Sen, Guy, N., Ozacar, M., 2017. Photocatalytic efficiencies of Ni, Mn, Fe and Ag doped ZnO nanostructures synthesized by hydrothermal method: The synergistic/antagonistic effect between ZnO and metals. J. Photochem. Photobiol. A Chem. 341, 39–50. https://doi.org/10.1016/j.jphotochem.2017.03.027.

Venkatesan, M., Fitzgerald, C.B., Lunney, J.G., Coey, J.M.D., 2004. Anisotropic Ferromagnetism in Substituted Zinc Oxide 15–18. https://doi.org/10.1103/PhysRevLett.93.177206

Wang, Y., Hao, X., Wang, Z., Dong, M., Cui, L., 2020. Facile fabrication of Mn2+- doped ZnO photocatalysts by electrospinning. R. Soc. Open Sci. 7. https://doi.org/10.1098/rsos.191050.

Wellia, D.V., Chi, Q., Alam, M., Hwa, K., Mariana, T., Thatt, T., Tan, Y., 2011. Experimental and theoretical studies of Fe-doped TiO2 films prepared by peroxo sol-gel method. Appl. Catal. A Gen. 401, 98–105. https://doi.org/10.1016/j.apcata.2011.05.003.

Wojnarowicz, J., Mukhovskyi, R., Pietrzykowska, E., Kusnieruk, S., Mizeracki, J., Lojkowski, W., 2016. Microwave solvothermal synthesis and characterization of manganese-doped ZnO nanoparticles. Beilstein J. Nanotechnol 7, 721–732. https://doi.org/10.3762/bjnano.7.64.

Wu, B., Li, J., Li, Q., 2019. Preparation and photoluminescence behavior of Mn-doped nano-ZnO. Optik (Stuttg). 188, 205–211. https://doi.org/10.1016/j.ijleo.2019.05.037.

Wu, C., Shen, L., Yu, H., Zhang, Y., Huang, Q., 2012. Solvothermal synthesis of Cu-doped ZnO nanowires with visible light-driven photocatalytic activity. Mater. Lett. 74, 236–238. https://doi.org/10.1016/j.matlet.2012.01.125.

Wu, C., Shen, L., Zhang, Y., Huang, Q., 2011. Solvothermal synthesis of Cr-doped ZnO nanowires with visible light-driven photocatalytic activity. Mater. Lett. 65, 1794–1796. https://doi.org/10.1016/j.matlet.2011.03.070.

Wu, Y., Kang, J., Liu, F., 2008. Pressure induced wurtzite-to-zinc blende phase transition in ZnO at finite temperature. J. Mater. Res. 23, 3347–3352. https://doi.org/10.1557/jmr.2008.0410.

Xu, J., Li, M., Yang, L., Qiu, J., Chen, Q., Zhang, X., Feng, Y., Yao, J., 2020. Synergy of Ni dopant and oxygen vacancies in ZnO for efficient photocatalytic depolymerization of sodium lignosulfonate. Chem. Eng. J. 394,. https://doi.org/10.1016/j.cej.2020.125050 125050.

Xu, K., Liu, C., Chen, R., Fang, X., Wu, X., Liu, J., 2016. Structural and room temperature ferromagnetic properties of Ni doped ZnO nanoparticles via low-temperature hydrothermal method. Phys. B Phys. Condens. Matter 502, 155–159. https://doi.org/10.1016/j.physb.2016.07.017.

Ye, Z., Lu, H., Geng, Y., Gu, Y., Xie, Z., Zhang, Y., Sun, Q., Ding, S., 2013. Structural, electrical, and optical properties of Ti-doped ZnO films fabricated by atomic layer deposition. Nanoscale Res. Lett. 8, 1–6. https://doi.org/10.1186/1556-276X-8-108.

Yi, S., Cui, J., Li, S., Zhang, L., Wang, D., Lin, Y., 2014. Applied Surface Science Enhanced visible-light photocatalytic activity of Fe/ZnO for rhodamine B degradation and its photogenerated charge transfer properties. Appl. Surf. Sci. 319, 230–236. https://doi.org/10.1016/j.apsusc.2014.06.151.

Yildirim, O.A., Arslan, H., Sönmezoğlu, S., 2016. Facile synthesis of cobalt-doped zinc oxide thin films for highly efficient visible light photocatalysts. Appl. Surf. Sci. 390, 111–121. https://doi.org/10.1016/j.apsusc.2016.08.069.

Yin, Q., Qiao, R., Li, Z., Li, X., Zhu, L., 2015. Hierarchical nanostructures of nickel-doped zinc oxide : Morphology controlled

synthesis and enhanced visible-light photocatalytic activity. J. Alloys Compd. 618, 318–325. https://doi.org/10.1016/j.jallcom.2014.08.087.

Yoshimura, M., Byrappa, K., 2008. Hydrothermal processing of materials: Past, present and future. J. Mater. Sci. 43, 2085–2103. https://doi.org/10.1007/s10853-007-1853-x.

Yu, X., Meng, D., Liu, C., 2014. Enhanced photocatalytic activity of Fe-doped ZnO nanoparticles synthesized via a two-step sol-gel method. J Matter Sci Mater Electron 25, 3920–3923. https://doi.org/10.1007/s10854-014-2107-8.

Yuliarto, B., Gumilar, G., Luh, N., Septiani, W., 2015. SnO2 Nanostructure as Pollutant Gas Sensors: Synthesis, Sensing Performances, and Mechanism. Adv. Mater. Sci. Eng. 2015. https://doi.org/10.1155/2015/694823.

Yumak, A., Turgut, G., Kamoun, O., Ozisik, H., Deligoz, E., 2015. Stability and morphology-dependence of Sc3 + ions incorporation and substitution kinetics within ZnO host lattice. Mater. Sci. Semicond. Process. 39, 103–111. https://doi.org/10.1016/j.mssp.2015.04.010.

Yusof, N.A.A., Zain, N.M., Pauzi, N., 2019. International Journal of Biological Macromolecules Synthesis of ZnO nanoparticles with chitosan as stabilizing agent and their antibacterial properties against Gram-positive and Gram- negative bacteria. Int. J. Biol. Macromol. 124, 1132–1136. https://doi.org/10.1016/j.ijbiomac.2018.11.228.

Zarlaida, F., Adlim, M., 2017. Gold and silver nanoparticles and indicator dyes as active agents in colorimetric spot and strip tests for mercury(II) ions: a review. Microchim. Acta 184, 45–58. https://doi.org/10.1007/s00604-016-1967-4.

Zhang, X., Chen, Y., Zhang, S., Qiu, C., 2017. High photocatalytic performance of high concentration Al-doped ZnO nanoparticles. Sep. Purif. Technol. 172, 236–241. https://doi.org/10.1016/j.seppur.2016.08.016.

Zhao, Z., Wang, M., Zhang, H., 2016. Microstructure and varistor properties of V-doped ZnO nanoparticles prepared by co-precipitation method. J. Mater. Sci. Mater. Electron. 27, 1777–1782. https://doi.org/10.1007/s10854-015-3953-8.

Zhong, Z.Y., Zhang, T., 2013. Microstructure and optoelectronic properties of titanium-doped ZnO thin films prepared by magnetron sputtering. Mater. Lett. 96, 237–239. https://doi.org/10.1016/j.matlet.2013.01.025.

Zhu, L., Xie, J., Cui, X., Shen, J., Yang, X., Zhang, Z., 2010. Photoelectrochemical and optical properties of N-doped TiO2 thin films prepared by oxidation of sputtered TiNx films. Vaccum 84, 797–802. https://doi.org/10.1016/j.vacuum.2009.10.040.